A review of the electrical properties of semiconductor nanowires: insights gained from

terahertz conductivity spectroscopy

You may also be interested in:

Intense terahertz radiation and their applications
H A Hafez, X Chai, A Ibrahim et al.

Terahertz conductivity in nanoscaled systems: effective medium theory aspects
P Kužel and H Nmec

Electronic properties of GaAs, InAs and InP nanowires studied by terahertz spectroscopy
Hannah J Joyce, Callum J Docherty, Qiang Gao et al.

One dimensional Si/Ge nanowires and their heterostructures for multifunctional applications—a review
Samit K Ray, Ajit K Katiyar and Arup K Raychaudhuri

A review on III–V core–multishell nanowires: growth, properties, and applications
Miquel Royo, Marta De Luca, Riccardo Rurali et al.

Ultrafast carrier dynamics and the role of grain boundaries in polycrystalline silicon thin films grown by molecular beam epitaxy
Lyubov V Titova, Tyler L Cocker, Sijia Xu et al.

The 2017 terahertz science and technology roadmap
S S Dhillon, M S Vitiello, E H Linfield et al.

THz emitters based on the photo-Dember effect
V Apostolopoulos and M E Barnes

Free-space broadband THz spectroscopy
P Y Han and X-C Zhang

Topical Review

A review of the electrical properties of semiconductor nanowires: insights gained from terahertz conductivity spectroscopy

Hannah J Joyce[1], Jessica L Boland[2], Christopher L Davies[2], Sarwat A Baig[1] and Michael B Johnston[2]

[1] Department of Engineering, University of Cambridge, Electrical Engineering Building, 9 JJ Thomson Avenue, Cambridge, CB3 0FA, UK
[2] Department of Physics, University of Oxford, Clarendon Laboratory, Parks Road, Oxford OX1 3PU, UK

E-mail: hannah.joyce@eng.cam.ac.uk

CrossMark

Abstract

Accurately measuring and controlling the electrical properties of semiconductor nanowires is of paramount importance in the development of novel nanowire-based devices. In light of this, terahertz (THz) conductivity spectroscopy has emerged as an ideal non-contact technique for probing nanowire electrical conductivity and is showing tremendous value in the targeted development of nanowire devices. THz spectroscopic measurements of nanowires enable charge carrier lifetimes, mobilities, dopant concentrations and surface recombination velocities to be measured with high accuracy and high throughput in a contact-free fashion. This review spans seminal and recent studies of the electronic properties of nanowires using THz spectroscopy. A didactic description of THz time-domain spectroscopy, optical pump–THz probe spectroscopy, and their application to nanowires is included. We review a variety of technologically important nanowire materials, including GaAs, InAs, InP, GaN and InN nanowires, Si and Ge nanowires, ZnO nanowires, nanowire heterostructures, doped nanowires and modulation-doped nanowires. Finally, we discuss how THz measurements are guiding the development of nanowire-based devices, with the example of single-nanowire photoconductive THz receivers.

Keywords: terahertz, nanowire, semiconductor, mobility, lifetime, ultrafast, contact-free

(Some figures may appear in colour only in the online journal)

1. Introduction

Semiconductor nanowires offer enormous versatility as nanoscale building blocks for the next generation of electronic devices. Nanowires are quasi-one dimensional nanostructures, with narrow diameters typically less than 300 nm and length-to-width aspect ratios typically greater than 10. Their free-standing nature and quasi one-dimensional geometry confer considerable advantages over conventional planar semiconductors: efficient strain relaxation [1], reduced cost and materials consumption [2], high surface area-to-

volume ratio, waveguiding properties [3, 4] and enhanced light trapping properties [2, 5, 6] to name a few. These unique properties are propelling new applications as diverse as nanowire-based tandem solar cells [7], single photon sources [3, 8, 9], photodetectors [10], nanoscale lasers [11, 12] and ultrahigh density wrap-gate transistors [13]. Nanowires are also a powerful platform for the study of fascinating fundamental physics. Recently for example, InAs nanowires [14] and InSb nanowires [15] have been employed in semiconductor–superconductor hybrid devices to investigate the existence of the Majorana fermion, a theoretically predicted

fundamental particle that is its own antiparticle and is of significance for quantum information processing.

Controlling the electrical properties of these nanowires is crucial to achieving the full potential of these remarkable materials. When engineering a nanowire-based device, the charge carrier lifetimes, mobilities, dopant concentrations and recombination mechanisms must be well understood and then tailored to optimise the device performance. Unfortunately, progress in understanding these crucial electrical properties has been hindered by the marked difficulties in performing electrical measurements on these nanoscale materials. Conventional electrical transport measurements, although appropriate for planar layers, are considerably more challenging to apply to nanowires. Somewhat ironically, it is the nanowire geometry that confers such enormous advantages that also makes it so difficult to perform conventional electrical transport measurements. In particular, Hall effect measurements, which are traditionally used to measure the electrical properties of planar semiconductors, require a particular contact geometry that is extremely challenging to apply to the quasi one-dimensional nanowire geometry [16].

In lieu of Hall effect measurements, field effect transistor (FET) measurements have become the most common method for probing the transport properties of semiconductor nanowires. Interpretation of FET measurements is, however, heavily influenced by the assumptions used to model the FET device [17–22]. It is not trivial to measure the gate capacitance, which is typically of the order of several hundred attoFarads, with sufficient sensitivity [23, 24]. Instead the gate capacitance is frequently estimated based on the geometry of the FET device [22] and uncertainties associated with the gate capacitance term can introduce systematic errors in the extraction of charge carrier mobility and concentration [17–20]. The uncertainty in the gate capacitance can also depend systematically on the nanowire diameter, distorting the apparent relationship between diameter and the determined properties [18]. The capture and release of carriers at interface trap states, which can manifest as gate hysteresis, is also difficult to measure and account for in the data analysis, and can strongly influence the extracted carrier mobility and carrier density [19]. Furthermore, the parasitic effect of contact resistance, if neglected in the data analysis, can lead to overestimation of charge carrier density [21, 22, 25].

To overcome these difficulties, research into alternative electrical measurement techniques has intensified. Sophisticated lithography processes have been developed to enable Hall effect magnetotransport measurements on single InAs [16, 22, 26] and InP nanowires [27]. Recently, thermoelectric measurements of the Seebeck coefficient have been employed to determine charge carrier concentrations and mobilities in nanowires [28–30]. Four-point probe measurements are frequently employed to provide measurements of nanowire resistivity, from which the charge carrier density can be inferred [31, 32]. Nevertheless, each of these contact-based techniques places specific requirements on the resistance and nature of the contacts (Ohmic or Schottky), and requires time-consuming and costly electron beam lithography and device processing. Furthermore, processing and electron beam

exposure can irreversibly modify the nanowire properties [26, 33], making it difficult to assess the nanowires' intrinsic properties and limiting the generality of the measurements. These problems slow the feedback cycle between nanowire growth and device development.

As a means of overcoming all these problems, contact-free probes of nanowire electrical properties have attracted significant attention [34, 35]. Terahertz (THz) conductivity spectroscopy is a relatively new contact-free and non-invasive technique that is ideally suited to nanowire electrical measurements. It is sensitive to carrier transport and dynamics at room temperature and is capable of sub-picosecond temporal resolution. Charge carrier *lifetimes*, *mobilities*, *dopant concentrations* and *surface recombination velocities* can be measured with high accuracy and with considerably higher throughput than achievable with traditional contact-based techniques. The recent proliferation of THz spectroscopy studies of Si, Ge and III–V nanowires are evidence of the strength of this technique.

In this review article, we will first introduce the THz frequency range and its relevance in the electronic characterisation of materials (section 2). In sections 3 and 4 we describe the principles of THz time-domain spectroscopy (THz-TDS) and optical pump–THz probe (OPTP) spectroscopy, respectively. The discussion will focus on the application of these techniques to nanowire samples and will describe how physical models of nanowire conductivity are applied to extract device-relevant electrical properties from the data (section 5). Studies of GaAs, InAs, InP, GaAs/AlGaAs core–shell nanowires, doped GaAs, modulation-doped GaAs/AlGaAs nanowires, Si, Ge and ZnO nanowires will be reviewed in section 6. Section 7 reviews pioneering strategies for achieving ultrafast THz measurements of single nanowires with nanometre spatial resolution. We conclude the review in section 8 with an example of how THz measurements are guiding the development of nanowire-based devices.

2. Conductivity in the THz frequency range

2.1. Significance of the THz range

The THz frequency range, often cited as 0.1–10 THz, corresponds to a free-space wavelength range of 3 mm–30 μm, wavenumbers of 3.3–333 cm^{-1} and low photon energies between 0.4 and 40 meV. The THz range falls between microwave and infra-red radiation in the electromagnetic spectrum, and its energy range is of the order of the thermal energy at room temperature ($k_B T = 25$ meV).

It is instructive to consider why the THz frequency range is of significance in inorganic semiconductors such as nanowires. Consider first the energetic range of THz radiation (0.4–40 meV), which spans the energies typical of quasiparticles and collective excitations. When THz frequency radiation is incident on a semiconductor, its alternating electric field $E(\omega)$ can stimulate the motion of charge carrier quasiparticles (e.g. free electrons and holes, surface plasmons, excitons and polarons) and excite collective excitations (e.g.

optical phonons). Consider also that the THz frequency range is of a similar order of magnitude to typical charge carrier scattering rates ($\sim 10^{13}\,\mathrm{s}^{-1}$) in inorganic semiconductors. Thus, THz spectroscopy probes the low energy electronic processes taking place in semiconductor nanowires, and is especially sensitive to the electrical conductivity of the nanowires.

There are two principal measurement regimes, (i) THz-TDS and (ii) OPTP spectroscopy, which respectively measure the AC electrical conductivity of the nanowires in their equilibrium and photoexcited states. THz-TDS is the simpler measurement. A typical THz-TDS system can measure the electrical conductivity $\sigma(\omega)$ of the sample as a function of frequency ω over a range of ~ 0.1 to $\sim 3\,\mathrm{THz}$. The conductivity spectrum $\sigma(\omega)$ provides more than just the magnitude of the conductivity: its spectral shape can reveal the mechanisms of charge transport in the material. Signatures of free carriers, surface plasmons and other phenomena can be readily identified from the spectra. The frequency of charge carrier scattering can be determined from the damping of spectral resonances.

OPTP spectroscopy is an extension of THz-TDS, in which the sample is photoexcited by an above-bandgap optical pulse. OPTP spectroscopy measures how $\sigma(\omega)$ changes in response to photoexcitation. It is a time-resolved technique and can therefore be used to measure charge carrier dynamics. Both THz-TDS and OPTP spectroscopy will be discussed in further detail in sections 3 and 4 respectively.

2.2. Complex conductivity and the dielectric response of nanowires

THz spectroscopy measures the response of the nanowires to an applied electric field, $E(\omega)$. The electric field is provided by electromagnetic radiation in the THz frequency range. The electrical response is quantified in terms of the nanowire conductivity $\sigma(\omega)$, which determines the current density $J(\omega)$ that results from an applied electric field:

$$J(\omega) = \sigma(\omega) E(\omega). \qquad (1)$$

The conductivity $\sigma(\omega)$ of the nanowires is generally frequency-dependent and complex, consisting of real and imaginary parts:

$$\sigma(\omega) = \sigma_{\mathrm{Re}}(\omega) + \mathrm{i}\sigma_{\mathrm{Im}}(\omega). \qquad (2)$$

The complex nature of the conductivity is easily explained by analogy with basic circuit theory: the real part is associated with the electrical resistance of the nanowires whereas the imaginary part is related to the reactance (capacitance or inductance) of the nanowires. At the relatively low frequencies typically accessible in FET and other contact-based measurements, the imaginary response is often negligible. At THz frequencies, however, the imaginary component becomes significant and meaningful.

The nanowires' dielectric function (or permittivity) is also complex and is given by

$$\epsilon_{\mathrm{nw}}(\omega) = \epsilon_1(\omega) + \mathrm{i}\epsilon_2(\omega). \qquad (3)$$

The dielectric function is related to the conductivity by

$$\epsilon_{\mathrm{nw}}(\omega) = \epsilon_{\mathrm{L,nw}}(\omega) + \frac{\mathrm{i}\sigma(\omega)}{\omega\epsilon_0}, \qquad (4)$$

where $\epsilon_0 = 8.854 \times 10^{-12}\,\mathrm{Fm}^{-1}$ is the dielectric permittivity of free space and $\epsilon_{\mathrm{L,nw}}(\omega)$ is the lattice component of the dielectric function. The lattice component is also frequency dependent. In semiconductor nanowires with a single transverse-optical (TO) phonon mode, $\epsilon_{\mathrm{L}}(\omega)$ is given by

$$\epsilon_{\mathrm{L,nw}}(\omega) = \epsilon_\infty + (\epsilon_{\mathrm{st}} - \epsilon_\infty)\frac{\omega_{\mathrm{TO}}^2}{\omega_{\mathrm{TO}}^2 - \omega^2 - \mathrm{i}\omega\gamma_{\mathrm{TO}}}, \qquad (5)$$

where ϵ_∞ is the high frequency (optical) dielectric constant of the nanowire material, ϵ_{st} is the low frequency (static) dielectric constant of the nanowire material, ω_{TO} is the TO-phonon frequency and γ_{TO} is the phonon damping constant. These parameters are well-known for many semiconductor materials [36]. THz frequencies accessible via THz-TDS and OPTP systems (~ 0.1 to $\sim 3\,\mathrm{THz}$) commonly lie below the TO-phonon frequency, where the lattice component can be approximated as $\epsilon_{\mathrm{L}}(\omega) = \epsilon_{\mathrm{st}}$. At mid-infra-red frequencies above the TO-phonon frequency, the lattice component can be approximated as $\epsilon_{\mathrm{L}}(\omega) = \epsilon_\infty(\omega)$.

By definition the complex refractive index $\tilde{n}(\omega)$ of the nanowires is related to their dielectric function by

$$\tilde{n}(\omega) = n(\omega) + \mathrm{i}k(\omega) = \sqrt{\epsilon_{\mathrm{nw}}(\omega)\mu}. \qquad (6)$$

The real part n is the refractive index associated with the phase delay of a wave as it passes through the nanowires, and the imaginary part is the extinction coefficient k associated with absorption. The permeability μ describes the magnetic response of the material, and hereafter will be set to $\mu = 1$ as our discussion is limited to nonmagnetic nanowires. From inspection of equations (4) and (6) it is clear that the complex refractive index $\tilde{n}(\omega)$, the dielectric response $\epsilon_{\mathrm{nw}}(\omega)$ and conductivity response $\sigma(\omega)$ contain equivalent information. THz-TDS is sensitive to each of these.

When the nanowires are photoexcited their complex refractive index, dielectric function and conductivity change. The conductivity changes by $\Delta\sigma(\omega)$, known as the photo-induced change in conductivity, or photoconductivity. Using equations (4) and (6) we find

$$\begin{aligned} \Delta\sigma(\omega) &= \mathrm{i}\omega\epsilon_0(\epsilon_{\mathrm{nw}}(\omega) - \epsilon_{\mathrm{nw}}^*(\omega)) \\ &= \mathrm{i}\omega\epsilon_0(\tilde{n}(\omega)^2 - \tilde{n}^*(\omega)^2), \end{aligned} \qquad (7)$$

where the superscripts * denote the values taken when the nanowires are photoexcited. OPTP spectroscopy is sensitive to $\Delta\sigma(\omega)$ and the photoinduced changes in $\tilde{n}(\omega)$ and $\epsilon_{\mathrm{nw}}(\omega)$.

3. Nanowire conductivity at equilibrium: THz-TDS

3.1. Basic principles

THz-TDS measures the electrical conductivity of the nanowires *at equilibrium*, that is, in their native state. The nanowire sample is probed with a short pulse $E(t)$ of
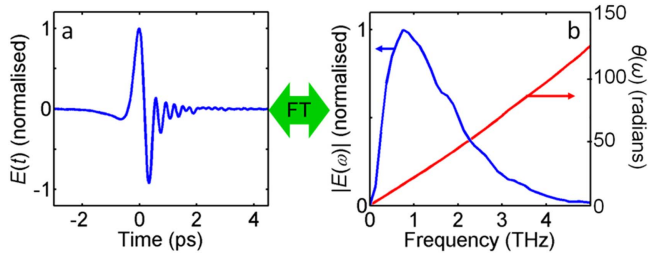
Figure 1. (a) Typical THz pulse $E(t)$ in the time domain and (b) its amplitude spectrum $|E(\omega)|$ and phase $\theta(\omega)$ in the frequency domain. The spectrum in (b) was obtained by performing a Fourier transform (FT) of the pulse in (a).
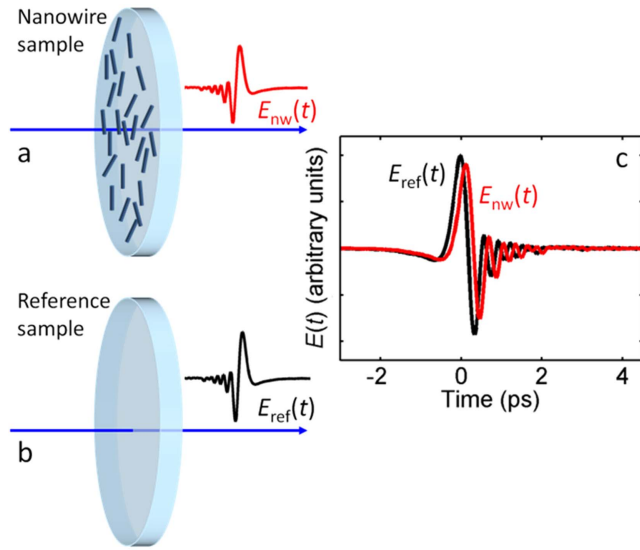
Figure 2. Schematic representation of THz-TDS measurements performed on (a) the nanowire sample and (b) the reference sample. The electric fields of the THz pulses measured after transmission are plotted in (c). The pulse transmitted through the nanowire sample $E_{nw}(t)$ undergoes absorption and a delay relative to the pulse transmitted through the reference sample $E_{ref}(t)$. Diagram is not to scale.

electromagnetic radiation in the THz frequency range. A typical incident THz pulse $E(t)$ is plotted in figure 1(a). In THz-TDS, the full electric field $E(t)$ is detected as a function of time, t, and hence the technique is termed 'TDS'. The frequency dependence of $E(t)$ can be obtained by performing a Fourier transform to yield the electric field $E(\omega)$ as a function of frequency ω. Figure 1(b) plots the corresponding amplitude spectrum $|E(\omega)|$ illustrating that the THz pulse is broadband containing frequency components between 0.1 and 4 THz.

THz-TDS is typically performed as a transmission measurement, whereby a THz pulse $E(t)$ is incident on the nanowire sample and the transmitted pulse $E_{nw}(t)$ is measured. The sample commonly consists of nanowires supported on a substrate, as illustrated in figure 2(a). While passing through the sample, the THz pulse undergoes absorption and a delay, due to its interaction with the nanowires and the underlying substrate. To calibrate the system response of the spectrometer, a reference pulse $E_{ref}(t)$ is also measured
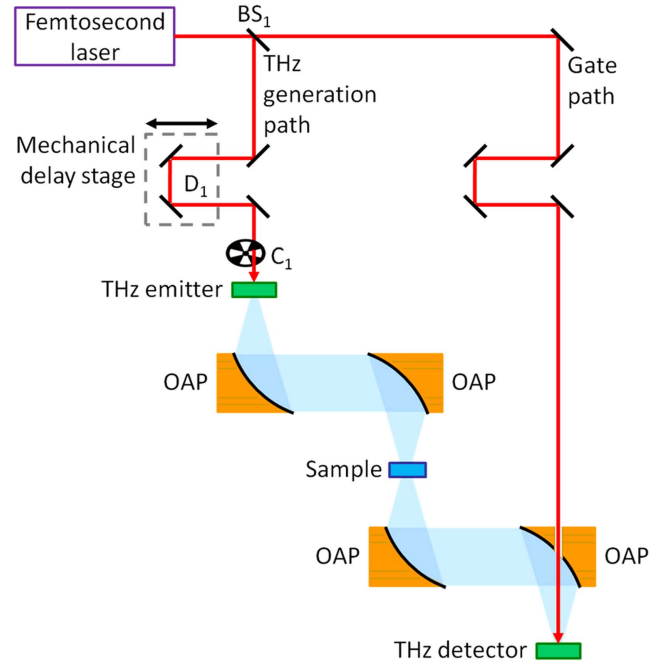
Figure 3. Schematic diagram of a typical THz-TDS system used to measure nanowire conductivity $\sigma(\omega)$. The femtosecond laser generates a beam of ultrashort laser pulses. The beam is divided by a beamsplitter (BS$_1$) into two paths: the THz generation path and the gate path. The THz generation path travels via a chopper (C$_1$) and via a moveable mechanical delay stage (D$_1$) which controls the time at which the THz pulse reaches the detector relative to the gate pulse. The THz pulse is generated at the THz emitter, focussed onto the sample by off-axis parabolic mirrors (OAPs), and detected at the THz detector.

through a reference substrate without the nanowires (figure 2(b)). The nanowire sample and reference spectra, $E_{nw}(\omega)$ and $E_{ref}(\omega)$, are obtained by performing Fourier transforms on the waveforms $E_{nw}(t)$ and $E_{ref}(t)$, respectively. The ratio $E_{nw}(\omega)/E_{ref}(\omega)$ corrects for the system response of the spectrometer, and yields the THz transmission function:

$$T(\omega) = \frac{E_{nw}(\omega)}{E_{ref}(\omega)}. \tag{8}$$

The THz transmission $T(\omega)$ is directly related to the nanowire conductivity $\sigma(\omega)$ as will be described in section 3.3.

3.2. Experimental system

Figure 3 illustrates a typical experimental THz-TDS system. A femtosecond laser (commonly a mode-locked Ti:sapphire laser of 800 nm centre wavelength) generates a train of ultrashort (<100 fs) optical pulses. The laser beam is divided by a beamsplitter (BS$_1$) into two paths: the THz generation path and the gate path.

The THz generation beam is focussed onto a THz emitter, where the incident optical pulse excites a THz pulse $E(t)$. The emitted THz pulse is collected and focussed onto the sample. The transmitted THz pulse is then collected and refocused onto the THz detector. The collection and focussing is achieved by off-axis parabolic mirrors, often arranged in two pairs as shown in figure 3.

The gate beam is also focussed onto the detector. The duration of the optical gate pulse (<100 fs) is much shorter than that of the THz pulse (~ 1 ps), so at the detector the optical gate pulse overlaps with the THz pulse over a very narrow temporal window. The detector measures the THz electric field only in this narrow temporal window when the two pulses overlap. This detection scheme is known as optical gating.

The THz generation beam travels via a mechanical delay stage (D_1). Moving the delay stage backwards increases the distance traversed by the THz generation beam, which delays the arrival of the THz pulse at the detector. For example, a 15 μm movement of the stage delays the THz pulse by 100 fs. This delay changes the time, t, at which the THz and gate pulses overlap at the detector, so that the detector samples a different region of the THz pulse. Therefore, by moving the delay stage, the electric field $E(t)$ of the THz pulse can be measured as a function of time t.

The entire beampath between the THz emitter and detector is enclosed within a chamber. This chamber is evacuated or filled with nitrogen or dry air during measurements to avoid absorption of the THz pulse by atmospheric water vapour. The THz generation beam is optically chopped (chopper C_1) and the THz pulse is detected using a lock-in amplifier referenced to the chopping frequency.

A salient feature of THz-TDS is its all-optical generation and detection of THz pulses. This feature enables the entire electric field $E(t)$ waveform to be mapped out with sub-picosecond temporal resolution, with both amplitude and phase information. The various techniques for the generation and detection of THz pulses are described thoroughly in previous reviews [37–40], so shall not be covered in detail here.

3.3. Extracting nanowire conductivity

As discussed in section 3.1, THz-TDS measures the transmission function $T(\omega)$ of the nanowires which is directly related to the conductivity $\sigma(\omega)$, dielectric function $\epsilon_{nw}(\omega)$ and complex refractive index $\tilde{n}(\omega)$ of the nanowires.

To extract $\sigma(\omega)$ from $T(\omega)$ it is necessary to consider the geometry of the nanowires, and the nature electromagnetic wave propagation through the sample. The characteristic dimensions of the nanowires are considerably smaller than the diffraction-limited spot size of the incident THz probe (~ 1 mm). It is therefore appropriate to use an effective medium theory, whereby the nanowires and surrounding medium (e.g. vacuum) are considered as a single composite layer l with an effective complex dielectric function $\epsilon_l(\omega)$, effective complex refractive index $\tilde{n}_l$, effective conductivity $\sigma_l(\omega)$ and effective thickness d_l. Different methods exist for extracting $\sigma(\omega)$ from $T(\omega)$. To exemplify how extraction of $\sigma(\omega)$ may be achieved, we will consider a sample where the composite nanowire layer is supported by the substrate of known complex refractive index $\tilde{n}_s$ and thickness d_s. This geometry is schematically illustrated in figure 4. Within the composite layer of thickness d_l, the nanowires occupy a
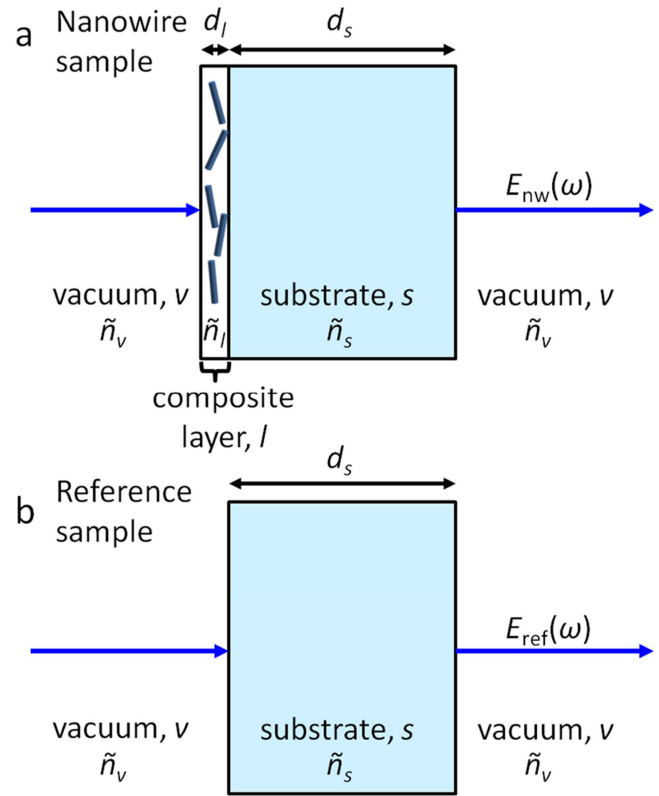
Figure 4. Model describing the interaction of the THz pulse with (a) a nanowire sample and (b) a reference sample in THz-TDS. In the nanowire sample the nanowires and surrounding medium (vacuum) are considered as a single composite layer l with an effective complex refractive index $\tilde{n}_l$ and effective thickness d_l. The nanowires are supported by the substrate of known complex refractive index $\tilde{n}_s$ and thickness d_s. Diagram is not to scale.

volume fraction f and the remainder of the volume is vacuum.

A theoretical expression for the transmission function $T(\omega)$ can be derived considering Fresnel transmission and reflection of a wave propagating through the sample at normal incidence. For the example geometry in figure 4, the theoretical expression is:

$$T(\omega) = \frac{E_{nw}(\omega)}{E_{ref}(\omega)} = \frac{2\tilde{n}_l(\tilde{n}_v + \tilde{n}_s)}{(\tilde{n}_v + \tilde{n}_l)(\tilde{n}_l + \tilde{n}_s)}$$
$$\times \exp\left(\frac{i\omega d_l}{c}(\tilde{n}_l - \tilde{n}_v)\right)\frac{FP_{vls}FP_{lsv}}{FP_{vsv}}, \quad (9)$$

where $\tilde{n}_i$ are the frequency-dependent complex refractive indices, c is the speed of light in vacuum and the subscripts v, l and s denote the vacuum, composite layer and substrate respectively. The Fabry–Pérot terms FP_{ijk} account for the echoes that arise from multiple internal reflections in the composite layer and in the substrate:

$$FP_{ijk} = \sum_{p=0}^{P}\left[r_{jk}r_{ji}\exp\left(\frac{2i\tilde{n}_j\omega d_j}{c}\right)\right]^p, \quad (10)$$

where $r_{ij} = (\tilde{n}_i - \tilde{n}_j)/(\tilde{n}_i + \tilde{n}_j)$ are the Fresnel reflection coefficients. The summation limit P is set by the number of

internal reflections recorded in the $E_{nw}(t)$ and $E_{ref}(t)$ waveforms.

Given the experimentally measured $T(\omega)$ and the known properties of the surrounding media (e.g. the substrate and vacuum), the theoretical expression for $T(\omega)$ (e.g. equation (9)) can be solved analytically or numerically to obtain $\tilde{n}_1$ and the complex dielectric function $\epsilon_1 = \tilde{n}_1^2$ of the composite layer [41].

In the case of nanowire samples, the composite layer containing the nanowires is often very thin compared to the wavelength of the THz radiation ($d_1 \ll \lambda_{THz}$, $P \to \infty$) and the underlying substrate is often very thick ($d_s > \lambda_{THz}$, $P = 0$), so expression (9) can be further simplified using the approximations outlined in [42]: $|\tilde{n}_1 \omega d_1/c| \ll 1$, $|\tilde{n}_v \omega d_1/c| \ll 1$, $\exp(i\tilde{n}_1 \omega d_1/c) = 1 + i\tilde{n}_1 \omega d_1/c$, $FP_{lsv} = 1$, $FP_{vsv}(\omega) = 1$ and $FP_{vls} = (1 - r_{ls} r_{lv} \exp(2i\tilde{n}_1 \omega d_1/c))^{-1}$. Applying these simplifications and noting that the complex refractive index of the vacuum is $\tilde{n}_v = 1$ yields

$$T(\omega) = \frac{(1 + \tilde{n}_s)}{(1 + \tilde{n}_s) - i(\tilde{n}_1^2 + \tilde{n}_s)\omega d_1/c}. \tag{11}$$

Rearranging the above and substituting $\epsilon_1 = \tilde{n}_1^2$ yields

$$\epsilon_1 = \frac{ic(1 + \tilde{n}_s)}{\omega d_1}\left(\frac{1}{T(\omega)} - 1\right) - \tilde{n}_s. \tag{12}$$

Thus, the effective complex dielectric function ϵ_1 of the composite layer can be calculated from $T(\omega)$.

Once ϵ_1 is determined is it possible to insert $\epsilon_1 = \epsilon_{L,1} + i\sigma_1/\omega\epsilon_0$ (equation (4)) into equation (12) and solve for $\sigma_1(\omega)$, the *effective* conductivity of the composite layer:

$$\sigma_1(\omega) = \frac{\epsilon_0 c(1 + \tilde{n}_s)}{d_1}\left(\frac{1}{T(\omega)} - 1\right) + i\omega\epsilon_0(\tilde{n}_s + \epsilon_{L,1}(\omega)). \tag{13}$$

In the case of a highly conductive sample, equation (13) can be approximated as

$$\sigma_1(\omega) = \frac{\epsilon_0 c(1 + \tilde{n}_s)}{d_1}\left(\frac{1}{T(\omega)} - 1\right). \tag{14}$$

Often one is interested in the conductivity of the nanowires alone, $\sigma(\omega)$, rather than the composite conductivity $\sigma_1(\omega)$. This $\sigma(\omega)$ may be calculated from $\sigma_1(\omega)$ by applying an appropriate effective medium theory, which will be discussed further in section 5.4. The conductivity is generally complex whereby the real part relates to the resistance of the nanowires and the imaginary part to the capacitance or inductance of the nanowires. Figure 5 exemplifies $\sigma(\omega)$ spectra obtained from THz-TDS measurements of a GaAs wafer and of GaAs nanowires.
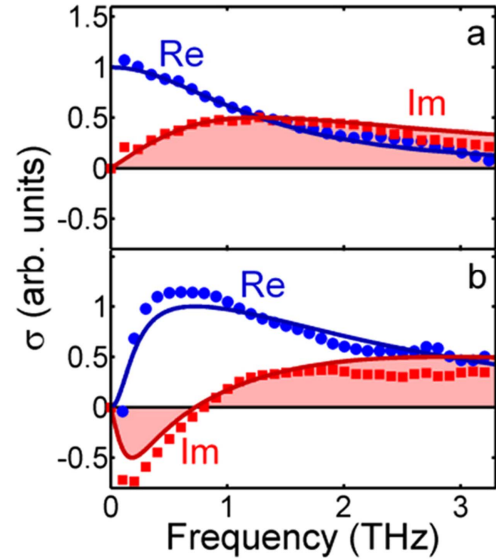
Figure 5. Equilibrium conductivity $\sigma(\omega)$ of (a) GaAs bulk wafer and of (b) GaAs nanowires measured by THz-TDS. Real (blue circles) and imaginary (red squares) parts of the measured conductivity are plotted. The lines are fits obtained using (a) the Drude model for the bulk and (b) the surface plasmon model for the nanowires.

4. Nanowire photoconductivity: OPTP spectroscopy

4.1. Basic principles

In contrast with THz-TDS, which probes equilibrium charge carrier transport, OPTP spectroscopy is a time-resolved technique and can therefore be used to probe charge carrier dynamics. Hence, OPTP spectroscopy is also known as time-resolved THz spectroscopy. OPTP spectroscopy measures the photoinduced change in conductivity $\Delta\sigma(\omega)$ resulting from photoexcitation of charge carriers.

OPTP spectroscopy is an extension of THz-TDS spectroscopy. In OPTP spectroscopy, an optical pump pulse with energy above the bandgap of the nanowires is used to photoexcite the nanowires before the arrival of the THz pulse, as illustrated in figure 6. The photoexcitation of mobile charge carriers increases the conductivity of the nanowires (photoconductivity), and hence reduces the transmission of the THz pulse.

With photoexcitation, the transmitted THz pulse is given by $E_{nw}^{ON}(t)$. Without photoexcitation, the transmitted THz pulse is given by $E_{nw}^{OFF}(t)$. The difference between transmitted electric fields $\Delta E(t)$ is conventionally defined as $\Delta E(t) = E_{nw}^{ON}(t) - E_{nw}^{OFF}(t)$. The fractional change in transmission $\Delta T/T$ due to photoexcitation can be calculated by performing Fourier transforms on the measured waveforms and then taking the following ratio:

$$\frac{\Delta T(\omega)}{T(\omega)} = \frac{\Delta E(\omega)}{E(\omega)} = \frac{E_{nw}^{ON}(\omega) - E_{nw}^{OFF}(\omega)}{E_{nw}^{OFF}(\omega)}. \tag{15}$$

The fractional change in transmission $\Delta T/T$ is directly related to the photoinduced change in nanowire conductivity $\Delta\sigma(\omega)$ as will be described in section 4.3. The time delay between the pump pulse and the THz probe pulse is known as
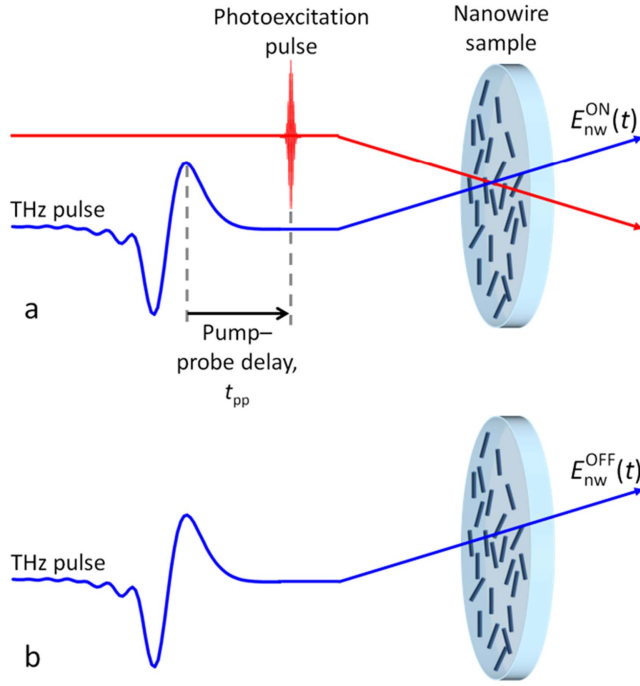
Figure 6. Schematic representation of the OPTP measurement. The sample is photoexcited by an above-bandgap optical pulse, then probed by the THz pulse which is transmitted with electric field $E_{nw}^{ON}(t)$. The time between the photoexcitation pulse and the peak of the THz pulse is known as the pump–probe delay t_{pp}. The reference measurement, $E_{nw}^{OFF}(t)$, is obtained without photoexcitation. Usually both the pump and THz probe meet the sample at normal incidence, but here they are drawn at an angle for clarity. Diagram is not to scale.

the pump–probe delay t_{pp}. By varying t_{pp}, it is possible to track how $\Delta\sigma(\omega)$ decays with time after photoexcitation.

4.2. Experimental system

A typical OPTP spectroscopy system is illustrated in figure 7. The OPTP spectrometer is a modified the THz-TDS system (figure 4), with the addition of an optical pump (photo-excitation) beam path. A second beamsplitter (BS$_2$) divides the laser beam into the pump beam path which is directed onto the sample. The pump beam travels via a mechanical delay stage (D$_2$) which controls the arrival time of the pump pulse at the sample surface, relative to the arrival time of the THz pulse. The difference in arrival times is known as the pump–probe delay, t_{pp}.

In OPTP studies of nanowires, amplified Ti:sapphire laser systems are often used to achieve high photoexcited carrier densities. At the sample surface the photoexcitation beam is typically expanded (rather than focussed), so that the photoexcitation spot size is larger than the THz spot size: this ensures a uniform photoexcited carrier density over the area probed by the THz pulse [43]. Otherwise, care must be taken in the data analysis to account for the frequency-dependent overlap of the pump and THz spots, as noted by Strait *et al* [44].

A chopper, C$_2$, is placed in the pump beam path so that the sample is modulated between its photoexcited and
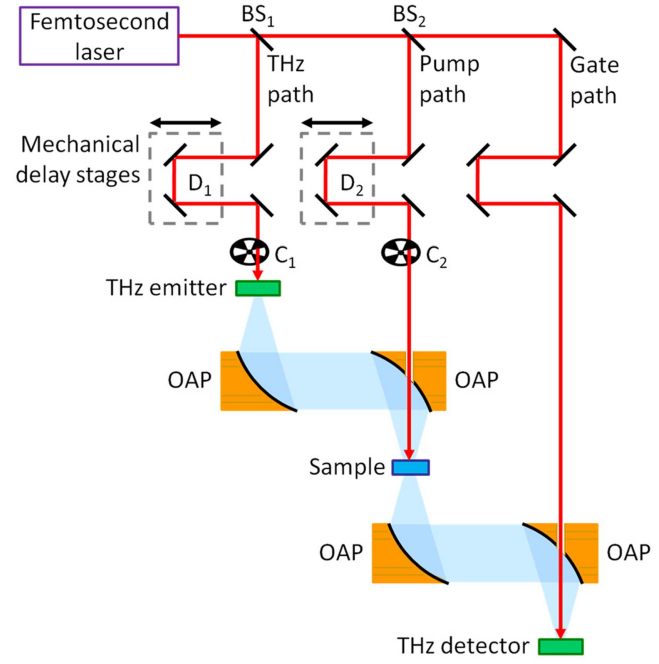
Figure 7. Schematic diagram of a typical OPTP system used to measure nanowire photoconductivity $\Delta\sigma(\omega)$. The system resembles the THz-TDS system of figure 3, except that the laser beam is divided by an additional beamsplitter (BS$_2$) into a third path: the optical pump path. The pump pulses travel to the sample via a chopper (C$_2$) and via a moveable mechanical delay stage (D$_2$) which controls the time at which the photoexcitation pulse reaches the sample relative to the THz pulse.

unexcited states. This modulates the transmitted THz pulse between $E_{nw}^{ON}(t)$ and $E_{nw}^{OFF}(t)$. In OPTP spectroscopy a dual lock-in technique is used for the detection of $\Delta E(t)$ and $E_{nw}^{OFF}(t)$. The first lock-in amplifier, similar to THz-TDS, receives the signal directly from the THz detector and is locked to the frequency of chopper C$_1$ in the THz generation beam. The second lock-in amplifier receives the signal from the first lock-in amplifier and is locked to the frequency of chopper C$_2$. The second amplifier records $\Delta E(t)$ whereas the first amplifier records the average of $E_{nw}^{ON}(t)$ and $E_{nw}^{OFF}(t)$:

$$\frac{1}{2}(E_{nw}^{ON}(t) + E_{nw}^{OFF}(t)) = E_{nw}^{OFF}(t) + \frac{1}{2}\Delta E(t). \qquad (16)$$

Commonly $\Delta E(t) \ll E_{nw}^{OFF}(t)$, so the waveform recorded by the first amplifier is approximately $E_{nw}^{OFF}(t)$. From the recordings taken by the first and second lock-in amplifiers, $E_{nw}^{OFF}(t)$, $E_{nw}^{ON}(t)$ and $\Delta E(t)$ can be determined. Figures 8(a) and (b) plot examples $E_{nw}^{OFF}(t)$ and $\Delta E(t)$ measurements. The photoinduced change $\Delta E(t)$ depends on both the THz delay t and the time after photoexcitation, t_{pp}.

The OPTP spectrometer can be used to obtain two different measurements: (i) photoconductivity spectra and (ii) photoconductivity decays. These are described below.

4.2.1. Photoconductivity spectra.
Spectral measurements record the fractional transmission $\Delta T(\omega)/T(\omega)$ as a function of frequency ω, at a fixed time after photoexcitation. In its simplest form, stage D$_2$ is held fixed
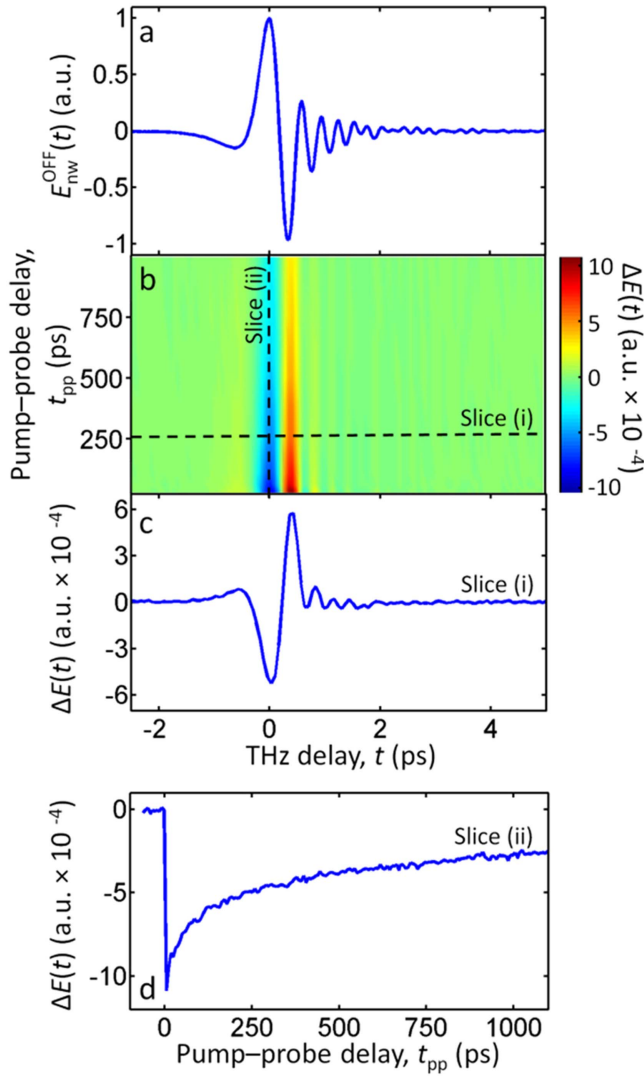
Figure 8. (a) THz electric field transmitted through a nanowire sample without photoexcitation, $E_{nw}^{OFF}(t)$, and (b) the corresponding photoinduced change in transmission $\Delta E(t)$ as a function of pump–probe delay time t_{pp}. Slices are taken (c) at fixed pump pump–probe delay time $t_{pp} = 250$ ps and (d) fixed at the THz peak. The measurement in (c) is used for determining photoconductivity spectra, whereas the measurement in (d) is a pump–probe decay curve used for determining photoconductivity decays. These nanowires were GaAs/AlGaAs core–shell–cap nanowires consisting of a 50 nm diameter GaAs core, a 16 nm AlGaAs shell and an outer 5 nm GaAs cap.

to maintain a constant pump–probe delay t_{pp}. The position of stage D_1 is varied to enable measurement of the entire THz waveforms $E_{nw}^{OFF}(t)$ and $\Delta E(t)$. Examples of $E_{nw}^{OFF}(t)$ and $\Delta E(t)$ are plotted in figures 8(a) and (c). The spectrum $\Delta T(\omega)/T(\omega)$ can be determined from $E_{nw}^{OFF}(t)$ and $\Delta E(t)$ by applying equation (15), and $\Delta T(\omega)/T(\omega)$ can in turn be directly converted into the photoconductivity $\Delta\sigma(\omega)$ of the nanowires (see section 4.3).

4.2.2. Photoconductivity decays. Rather than measure the entire THz waveform, these measurements record the fractional transmission $\Delta T/T$ at the peak of the THz pulse

only, and track how $\Delta T/T$ changes as a function of time after photoexcitation. Stage D_1 is held fixed so that the peak electric field of the THz pulse, $E_{nw}^{OFF,\ max}$, is measured at the THz detector. The position of stage D_2 is varied to increase the pump–probe delay t_{pp}. Then, ΔE is measured for each pump–probe delay t_{pp}, as exemplified in figure 8(d). This enables $\Delta T/T = \Delta E/E_{nw}^{OFF,\ max}$ to be determined as a function of t_{pp}.

4.3. Extracting nanowire photoconductivity

OPTP spectroscopy measures the relative photoinduced change in transmission $\Delta T/T$ through the nanowire sample, which is directly related to the photoconductivity $\Delta\sigma(\omega)$ of the nanowires. Calculation of $\Delta\sigma(\omega)$ requires consideration of the sample geometry, the absorption depth of the photo-excitation pulse, and the propagation of the THz pulse through sample with and without photoexcitation, as discussed in detail in [45]. As with THz-TDS spectroscopy, it is appropriate to use an effective medium theory as described in section 3.3.

To demonstrate how $\Delta\sigma(\omega)$ may be calculated from $\Delta T/T$, we will consider the simple sample geometry shown in figure 4(a). The substrate exhibits no photoconductivity response and the thin composite layer of nanowires is uniformly photoexcited. Considering wave propagation through this sample, a theoretical expression for $\Delta T/T$ can be derived:

$$\frac{\Delta T(\omega)}{T(\omega)} = \frac{E_{nw}^{ON}(\omega)}{E_{nw}^{OFF}(\omega)} - 1 = \frac{(\tilde{n}_v + \tilde{n}_l^*)(\tilde{n}_l^* + \tilde{n}_s)}{(\tilde{n}_v + \tilde{n}_l)(\tilde{n}_l + \tilde{n}_s)}$$
$$\times \exp\left(\frac{\mathrm{i}\omega d_l}{c}(\tilde{n}_l^* - \tilde{n}_l)\right)\frac{FP_{vls}^* FP_{lsv}^*}{FP_{vls} FP_{lsv}} - 1, \quad (17)$$

where $\tilde{n}_i$, c, d_l, FP_{ijk} are as defined in section 3.3, and the superscript $*$ denotes the values taken when the nanowires are photoexcited. The experimentally measured $\Delta T/T$, and the known values of $\tilde{n}_s$, $\tilde{n}_v$ and d_l can be substituted into the theoretical expression for $\Delta T/T$, leaving $\tilde{n}_l^*$ and $\tilde{n}_l$ as unknowns.

Often, the composite layer containing the nanowires is very thin ($d_l \ll \lambda_{THz}$, $P \to \infty$) and the underlying substrate is very thick ($d_s > \lambda_{THz}$, $P = 0$). In this case expression (17) can be further simplified using same approximations outlined in section 3.3 and noting that the complex refractive index of the vacuum is $\tilde{n}_v = 1$:

$$\frac{\Delta T(\omega)}{T(\omega)} = \frac{\mathrm{i}\omega d_l}{c}\frac{(\tilde{n}_l^{*2} - \tilde{n}_l^2)}{(1 + \tilde{n}_s)}. \quad (18)$$

The above can be rearranged to

$$\tilde{n}_l^{*2} - \tilde{n}_l^2 = -\frac{\mathrm{i}c(1 + \tilde{n}_s)}{\omega d_l}\frac{\Delta T(\omega)}{T(\omega)}, \quad (19)$$

to solve for the photoinduced change in complex dielectric function of the composite layer, $\tilde{n}_l^{*2} - \tilde{n}_l^2 = \epsilon_l^* - \epsilon_l$. Then, $\epsilon_l^* - \epsilon_l = \mathrm{i}\Delta\sigma_l/\omega\epsilon_0$, can be inserted into equation (19) to solve for $\Delta\sigma_l(\omega)$, the *effective* photoconductivity of the
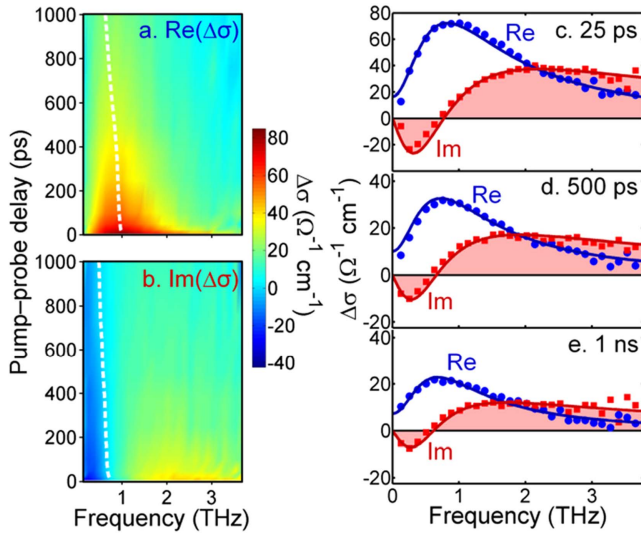
Figure 9. Frequency-dependent photoconductivity $\Delta\sigma(\omega)$ extracted from the raw data of figure 8. The sample was composed of GaAs/AlGaAs core–shell–cap nanowires. The colour maps of (a) and (b) plot photoconductivity at different times after photoexcitation, showing (a) real and (b) imaginary parts of $\Delta\sigma(\omega)$. The photoconductivity spectra of (c)–(e) were obtained at (c) 25 ps, (d) 500 ps and (e) 1 ns after photoexcitation, where the symbols are the measured data, the lines are fits obtained with a surface plasmon model, the blue circles are the real components and the red squares are the imaginary components. Reprinted with permission from [46]. Copyright 2014 American Chemical Society.

composite layer:

$$\Delta\sigma_1(\omega) = -\frac{\epsilon_0 c (1 + \tilde{n}_s)}{d_1} \frac{\Delta T(\omega)}{T(\omega)}. \tag{20}$$

In the above equation the effective photoconductivity $\Delta\sigma_1(\omega)$ is directly proportional to $\Delta T/T$. The proportionality between $\Delta\sigma_1(\omega)$ and $\Delta T/T$ is commonly utilised in analyses of OPTP studies.

Effective medium theories (to be described in section 5.4) can be applied to determine the photoconductivity of the nanowires alone. Figure 9 exemplifies $\Delta\sigma(\omega)$ spectra: these were obtained from the raw OPTP data plotted in figures 8(a) and (b). The magnitude of the $\Delta\sigma(\omega)$ spectra decays with time after photoexcitation as the photo-excited charge carrier population decays. Figure 10 illustrates a photoconductivity decay curve obtained from the raw pump–probe decay curve of figure 8(d).

5. Physical models of THz conductivity in nanowires

THz-TDS and OPTP spectroscopy yield the frequency-dependent complex conductivity spectra $\sigma(\omega)$ and photo-conductivity spectra $\Delta\sigma(\omega)$, respectively, of the nanowires. These spectra provide a wealth of information regarding the mechanisms of charge transport in the nanowires. Physical parameters of interest—such as charge carrier scattering rate γ, dc mobility μ and density N—may be obtained by fitting the measured spectra with physical models that describe the
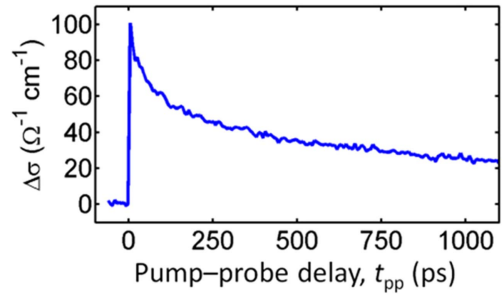
Figure 10. Photoconductivity decay obtained from the pump–probe decay curve of figure 8(d).

known relationship between the conductivity and these physical parameters. This section describes the models and methods most commonly applied to measurements of nanowires.

5.1. Drude model

The Drude model, also known as the Drude–Lorentz model, is a simple classical model of the frequency-dependent conductivity of metals and semiconductors. This model describes the motion of charge carriers under an applied alternating electric field $E(\omega)$. The charge carriers undergo scattering events that randomise their momentum with a scattering rate γ. According to the Drude model, the conductivity is given by

$$\sigma(\omega) = \frac{Ne^2}{m^*} \frac{i}{\omega + i\gamma}, \tag{21}$$

where N is the charge carrier density, e is the electronic charge (1.602×10^{-19} C) and m^* is the effective mass of the charge carriers. The inverse of the momentum scattering rate, γ^{-1}, is the scattering time, the average time between consecutive scattering events. The dc charge carrier mobility μ is related to the scattering rate γ by

$$\mu = \frac{e}{m^* \gamma}. \tag{22}$$

An example spectrum corresponding to the Drude model is plotted in figure 11(a). It features a peak in its real part at zero frequency and a peak in its imaginary part at $\omega = \gamma$. This spectral shape describes the conductivity of bulk samples well (e.g. figure 5(a)), but does not reproduce the typical spectra obtained from nanowires, such as those of figures 5(b) and 9. The experimental nanowire spectra feature a negative imaginary component at low frequencies which cannot be fitted with the Drude model.

The Drude model does not account for several transport phenomena that can arise due to the finite nanoscale dimensions of the nanowires, including backscattering of electrons at nanowire surfaces, surface depletion and accumulation fields at the boundaries of the nanowires, carrier localisation and the polarisability of the nanowires [47]. Consequently the nanowire conductivity spectra deviate from the standard Drude response. For this reason, researchers have looked to extensions of the Drude model that more accurately describe
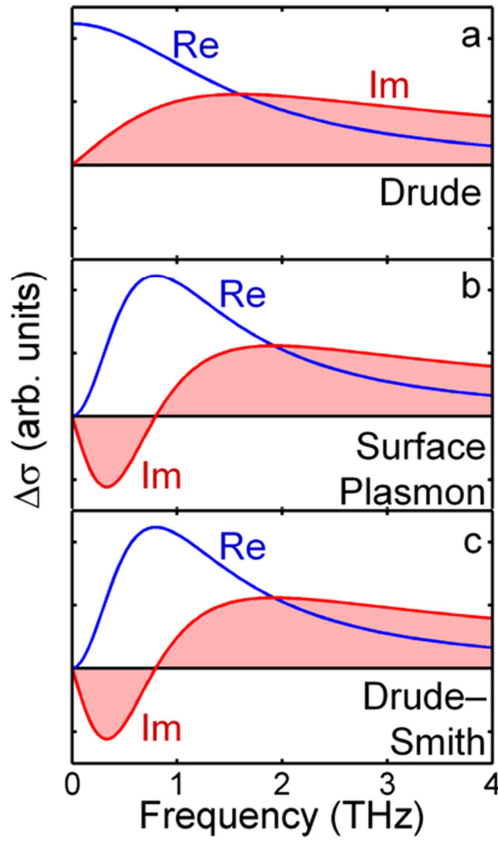
Figure 11. Example conductivity spectra determined by different physical models of nanowire conductivity: (a) Drude response with $\gamma = 10^{13}$ s^{-1}, (b) surface plasmon response with $\gamma = 10^{13}$ s^{-1} and $\omega_0 = 5 \times 10^{12}$ rad s^{-1}, and (c) Drude–Smith model with $\gamma_{DS} = 5 \times 10^{12}$ s^{-1} and $c_1 = -1$.

the conductivity response of the nanowires. These include the surface plasmon model and the Drude–Smith model, which are discussed next.

5.2. Surface plasmon model

The surface plasmon model is a generalisation of the Drude model in which the carriers are also subject to an electrostatic restoring force. A plasmon model was proposed by Nienhuys and Sundström [48] to describe the THz conductivity spectra of particles that are small compared to the THz wavelength, in which carriers cannot travel beyond the boundaries of the particles. Under an electric field, as applied by a THz pulse, electrons and holes are driven in opposite directions. The result is a net excess of positive charge on one side of the particle, and negative charge on the opposite side, creating an electric dipole. The electric field associated with the dipole opposes the applied electric field, and is known as a depolarisation field, E_D. Depolarisation fields are shown schematically in figures 12(a) and (b), for applied electric fields oriented parallel and perpendicular to the nanowire axis, respectively. The depolarisation field acts as an electrostatic restoring force, causing the carriers to undergo harmonic oscillation. The shape of the surface plasmon response is a
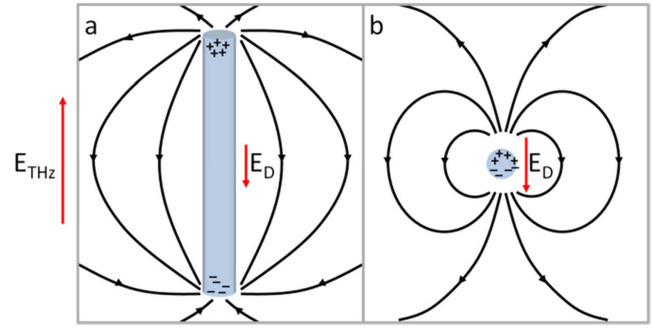
Figure 12. A schematic diagram illustrating the depolarisation field E_D arising from the accumulation of charges when an electric field E_{THz} is applied (a) parallel to the nanowire axis and (b) perpendicular to the nanowire axis.

modified Drude response that follows a Lorentzian function:

$$\sigma(\omega) = \frac{Ne^2}{m^*} \frac{i\omega}{\omega^2 - \omega_0^2 + i\omega\gamma}, \qquad (23)$$

where ω_0 is the resonant frequency and the other parameters follow the Drude definitions. The surface plasmon spectrum (figure 11(b)) features a negative imaginary part at low frequencies, as observed in experimental spectra from nanowires. The scattering rate γ is related to the charge carrier mobility μ by equation (22). The resonant frequency follows

$$\omega_0 = \sqrt{g \frac{Ne^2}{\epsilon_0 m^*}}, \qquad (24)$$

where g is a factor related to the geometry and the dielectric constants of the nanowires and surrounding medium. According to equation (24), the resonant frequency scales with the square root of the carrier concentration, a key attribute of plasmon modes.

Surface plasmon modes are well characterised for metallic nanostructures, for which the resonant plasmon frequencies lie in the ultraviolet, visible and near infra-red ranges. Semiconductor nanowires feature lower carrier densities than metallic nanostructures and consequently exhibit resonance at lower frequencies corresponding to the THz range. THz surface plasmon modes have been observed in a variety of semiconductor nanowires, including Ge nanowires [44] and III–V nanowires [49–51]. Photoconductivity spectra of these nanowires exhibit the shift in ω_0 with carrier density (equation (24)) that is characteristic of surface plasmon modes. Figure 13 exemplifies this shift: the plasmon resonance of GaAs nanowires shifts to higher frequencies with increasing photoexcitation fluence, or equivalently, with increasing photoexcited carrier density. When fitting spectra with equation (23), N and γ are used as adjustable parameters. Fitting the data thus enables the determination of N and γ, and also μ via equation (22). In the fit, the parameter ω_0 can be also be adjusted, or can be fixed relative to N according to equation (24).

In the analysis of photoconductivity spectra, the relationship between ω_0 and $\sqrt{N}$ can be exploited for
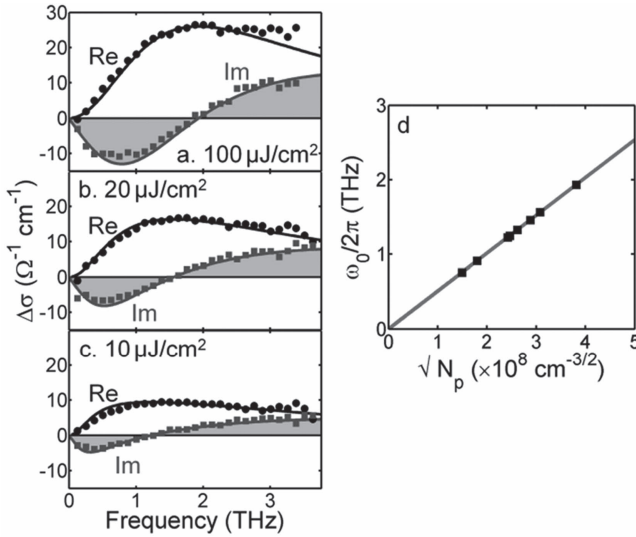
Figure 13. Dependence of photoconductivity spectra on carrier density in GaAs nanowires. The photoconductivity spectra were obtained 2 ps after photoexcitation at fluences of (a) 100, (b) 20 and (c) 10 μJ cm^{-2}. Spectra were fitted with the surface plasmon model. At the resonant frequency ω_0, the real part of $\Delta\sigma(\omega)$ reaches a maximum and the imaginary part of $\Delta\sigma(\omega)$ is zero. The charge carrier density increases with increasing fluence, accompanied by a shift in the resonant frequency ω_0. (d) Surface plasmon resonance frequencies ω_0 versus the square root of the photoexcited carrier density N_p. Reprinted with permission from [51]. Copyright 2013 Institute of Physics.

determination of the equilibrium carrier density N_{eq} [51], as follows. Photoconductivity spectra measure the difference in conductivity between the photoexcited and equilibrium states:

$$\Delta\sigma(\omega) = \sigma_p(\omega) - \sigma_{eq}(\omega), \quad (25)$$

where $\sigma_p(\omega)$ is the total conductivity when photoexcited and $\sigma_{eq}(\omega)$ is the conductivity at equilibrium without photoexcitation. In many undoped samples, $\sigma_{eq}(\omega)$ is negligible, such as in the GaAs nanowire samples analysed in figure 13. However, values of N_{eq} can be significant in doped nanowires and in nanowires with small bandgaps, giving rise to a significant $\sigma_{eq}(\omega)$. According to the surface plasmon model:

$$\sigma_p(\omega) = \frac{(N_p + N_{eq})e^2}{m^*}\frac{i\omega}{\omega^2 - \omega_{0,N_p+N_{eq}}^2 + i\omega\gamma} \quad (26)$$

and

$$\sigma_{eq}(\omega) = \frac{(N_{eq})e^2}{m^*}\frac{i\omega}{\omega^2 - \omega_{0,N_{eq}}^2 + i\omega\gamma}, \quad (27)$$

where N_p is the density of photoexcited carriers, $\omega_{0,N_p+N_{eq}} = \sqrt{g(N_p + N_{eq})e^2/\epsilon_0 m^*}$ and $\omega_{0,N_{eq}} = \sqrt{gN_{eq}e^2/\epsilon_0 m^*}$. Fitting $\Delta\sigma(\omega)$ spectra with equations (25)–(27) can yield an accurate value of N_{eq}. The accuracy can be improved further by performing a global fit over multiple spectra taken with different photoexcited carrier densities N_p. In the global fit g and N_{eq} are used as global fitting parameters, that is, parameters held fixed for all spectra. This approach was taken in [51] to determine the

doping concentrations in InAs and InP nanowires and has been since used to determine doping concentrations in modulation-doped [52] and shell-doped GaAs nanowires and in n-doped Si nanowires [53].

5.3. Drude–Smith model

The Drude–Smith model [54] is a phenomenological extension of the Drude model that was developed to describe materials in which localisation and disorder disrupt charge carrier transport. Unlike the Drude model, which describes only isotropic carrier scattering, the Drude–Smith model can describe scattering in preferential directions. The expression for conductivity is given by

$$\sigma(\omega) = \frac{Ne^2}{m^*}\frac{i}{\omega + i\gamma_{DS}}\left[1 + \sum_{p=1}^{\infty}\frac{c_p}{(1 - i\omega/\gamma_{DS})^p}\right], \quad (28)$$

where γ_{DS} is the Drude–Smith scattering rate and c_p is the fraction of the carrier's initial velocity retained after scattering event p. The c_p parameter, known as the persistence of velocity parameter, accounts for the anisotropy of scattering. For elastic collisions c_p is the expectation value $\langle \cos\theta \rangle$ where θ is the scattering angle. For completely isotropic Drude-like scattering $c_p = 0$, for forward scattering c_p is positive, for backward scattering c_p is negative, for totally forward scattering $c_p = 1$ and for complete backscattering $c_p = -1$. The infinite summation in equation (28) is usually truncated after the first term, $p = 1$, known as the single-scattering approximation. Figure 11(c) plots an example spectrum obtained using the Drude–Smith model with the single-scattering approximation. Under the single-scattering approximation, the dc electron mobility is given by

$$\mu = (1 + c_1)\frac{e}{m^*\gamma_{DS}}. \quad (29)$$

However, some publications use

$$\mu = \frac{e}{m^*\gamma_{DS}}, \quad (30)$$

which can overestimate the mobility.

The Drude–Smith model can reproduce the negative imaginary component observed in nanowire spectra, and has therefore found widespread applicability in the analysis of the THz conductivity spectra of nanowires [55–57]. The parameters N, γ_{DS}, and c_1 are used as adjustable parameters when fitting the experimental data. The fitted parameter c_1 is generally negative indicating preferential backscattering of electrons in the nanowires. Backscattering may arise when electrons bounce off the nanowire surfaces and when electrons are subject to Coulombic restoring forces. The fitted c_1 is used as a measure of carrier localisation in the nanowires, where a value closer to $c_1 = -1$ indicates greater localisation. Figure 14 exemplifies a Drude–Smith fit to data obtained from ZnO nanowires.

The primary criticism of the Drude–Smith model concerns the validity of the single-scattering approximation. The physical interpretation of this approximation is that scattering is only anisotropic for the first scattering event, and is
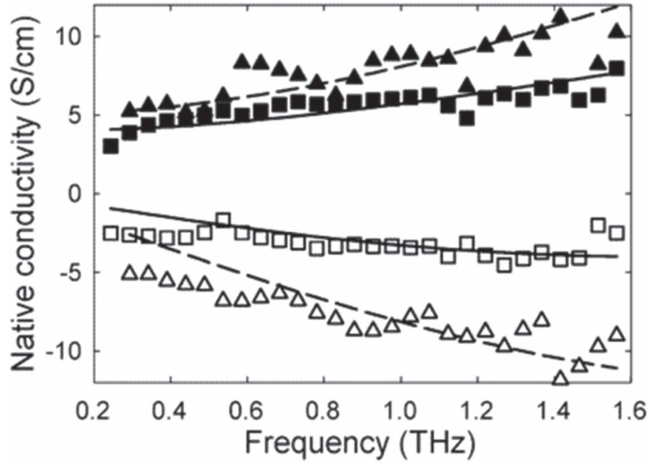
Figure 14. Equilibrium conductivity $\sigma(\omega)$ of a ZnO film (squares) and of an ensemble of ZnO nanowires (triangles) measured by THz-TDS. Real (solid symbols) and imaginary (open symbols) parts of the measured conductivity are plotted. The lines are fits obtained using the Drude–Smith model for the film (solid lines) and the nanowires (dashed lines). Reprinted with permission from [55]. Copyright 2006 American Chemical Society.

isotropic thereafter. The physical origin of this approximation is not well-justified, which limits the physical insight gained from Drude–Smith fits. Interestingly, the Drude–Smith and surface plasmon models give equivalent spectra if $c_1 = -1$, $\gamma_{DS} = \frac{1}{2}\gamma$ and $\omega_0 = \gamma_{DS}$, as observed comparing figures 11(b) and (c). Monte Carlo simulations carried out by Němec *et al* showed that the localisation of free carriers in nanoparticles gives rise to the phenomenological results of the Drude–Smith model [58].

5.4. Effective medium theories

THz-TDS and OPTP techniques directly measure the conductivity and dielectric responses of the composite layer containing the nanowires. As discussed in section 3.3, the response of the composite layer can be analysed using an effective medium theory. Effective medium theories relate the dielectric function ϵ_l of the composite layer to the dielectric function ϵ_{nw} of the particles (nanowires), the dielectric function ϵ_h of the host medium (often vacuum) in which the nanowires are embedded, and the volume fraction f occupied by the nanowires. When applied in reverse, a 'reverse effective medium theory' enables extraction of ϵ_{nw} from known values of ϵ_l, ϵ_h and f. Using ϵ_l it is possible to extract the complex dielectric function of the constituent nanowires ϵ_{nw}, and hence the conductivity of the nanowires alone $\sigma(\omega)$.

The two most commonly used effective medium theories are the Maxwell–Garnett and the Bruggeman effective medium theories [59, 60]. The Maxwell–Garnett formula is given by

$$f\frac{\epsilon_{nw} - \epsilon_h}{\epsilon_{nw} + \kappa\epsilon_h} - \frac{\epsilon_l - \epsilon_h}{\epsilon_l + \kappa\epsilon_h} = 0, \qquad (31)$$

which can be rearranged to solve for ϵ_{nw}:

$$\epsilon_{nw} = \epsilon_h\left(\frac{f(\epsilon_l + \kappa\epsilon_h) + \kappa(\epsilon_l - \epsilon_h)}{f(\epsilon_l + \kappa\epsilon_h) - (\epsilon_l - \epsilon_h)}\right), \qquad (32)$$

or ϵ_l:

$$\epsilon_l = \epsilon_h\left(\frac{\kappa f(\epsilon_{nw} - \epsilon_h) + (\epsilon_{nw} + \kappa\epsilon_h)}{-f(\epsilon_{nw} - \epsilon_h) + (\epsilon_{nw} + \kappa\epsilon_h)}\right). \qquad (33)$$

Maxwell–Garnett effective medium theory does not provide reliable results if percolation pathways exist for charge transport between nanowires. However, most nanowire samples reported to date feature well-isolated single-crystalline nanowires, so inter-nanowire percolative transport is not considered significant in these samples. The Maxwell–Garnett effective medium theory is also not suitable if the volume fraction f is large. In the case of large f, the Bruggeman approximation provides more accurate results:

$$f\frac{\epsilon_{nw} - \epsilon_l}{\epsilon_{nw} + \kappa\epsilon_l} + (1 - f)\frac{\epsilon_h - \epsilon_l}{\epsilon_h + \kappa\epsilon_l} = 0, \qquad (34)$$

which can be rearranged to solve for ϵ_{nw}:

$$\epsilon_{nw} = \epsilon_l\left(\frac{f(\epsilon_h + \kappa\epsilon_l) - (1 - f)\kappa(\epsilon_h - \epsilon_l)}{f(\epsilon_h + \kappa\epsilon_l) + (1 - f)(\epsilon_h - \epsilon_l)}\right). \qquad (35)$$

In the above, κ is related to the depolarisation factor which depends on the nanowire geometry and orientation relative to the electric field polarisation of the THz pulse: $\kappa = 2$ for spherical particles and $\kappa = 1$ for infinitely long cylinders oriented with their axes perpendicular to the THz electric field [47, 55].

A number of other effective medium theories exist, each based on different assumptions and suitable under particular circumstances [61, 62]. The choice of effective medium theory depends on the geometry and composition of the sample. Baxter and Schmuttenmaer, for example, applied the Bruggeman approximation in reverse (equation (35)) with $\kappa = 1$, to calculate complex dielectric function of ZnO nanowires oriented with their axes collinear with the incident THz pulse [55]. Ponseca *et al* employed the Maxwell–Garnett effective medium theory with $\kappa = 1$ to fit measured photoconductivity spectra obtained from a composite layer of InP nanowires in a PDMS matrix [63]. Kužel and Němec have recently published a thorough analysis of the application of effective medium theories in OPTP studies of nanostructured samples such as nanowires [47].

Both Maxwell–Garnett and Bruggeman effective medium theories are derived considering the local depolarisation fields arising in the nanowires (figure 12) under the applied electric field. This provides a link to the surface plasmon model, which is similarly based on the depolarisation fields in these nanowires. Hendry *et al* demonstrated that the Maxwell–Garnett effective medium relationship can reproduce resonances in THz spectra [64]. To highlight this link we consider the Maxwell–Garnett approximation for a sample in which the nanowires are non-conducting and for a sample of identical composition in which the nanowires are conducting.

In the non-conducting case, $\epsilon_{nw} = \epsilon_{L,nw}$ and $\epsilon_l = \epsilon_{L,l}$, and equation (33) becomes

$$\epsilon_{L,l} = \epsilon_h \left(\frac{\kappa f (\epsilon_{L,nw} - \epsilon_h) + (\epsilon_{L,nw} + \kappa \epsilon_h)}{-f (\epsilon_{L,nw} - \epsilon_h) + (\epsilon_{L,nw} + \kappa \epsilon_h)} \right). \quad (36)$$

In the conducting case, $\epsilon_{nw} = \epsilon_{L,nw} + i\sigma/\omega\epsilon_0$ and $\epsilon_l = \epsilon_{L,l} + i\sigma_l/\omega\epsilon_0$ and equation (33) becomes

$$\epsilon_{L,l} + i\sigma_l/\omega\epsilon_0 = \epsilon_h$$
$$\times \left(\frac{\kappa f (\epsilon_{L,nw} + i\sigma/\omega\epsilon_0 - \epsilon_h) + (\epsilon_{L,nw} + i\sigma/\omega\epsilon_0 + \kappa \epsilon_h)}{-f (\epsilon_{L,nw} + i\sigma/\omega\epsilon_0 - \epsilon_h) + (\epsilon_{L,nw} + i\sigma/\omega\epsilon_0 + \kappa \epsilon_h)} \right). \quad (37)$$

Combining equations (36) and (37) and solving for σ_l yields:

$$\sigma_l(\omega) = \frac{(A/B)\sigma}{B + (1 - f)i\sigma/\omega\epsilon_0}, \quad (38)$$

where constants A and B are given by

$$A = f\epsilon_h^2 (\kappa + 1)^2 \quad (39)$$

and

$$B = -f (\epsilon_{L,nw} - \epsilon_h) + (\epsilon_{L,nw} + \kappa \epsilon_h). \quad (40)$$

Substituting the Drude equation (21) for σ into equation (38) gives

$$\sigma_l(\omega) = \frac{A}{B^2} \frac{Ne^2}{m^*} \frac{i\omega}{\omega^2 - \omega_0^2 + i\omega\gamma}, \quad (41)$$

where

$$\omega_0 = \sqrt{\frac{(1 - f)}{B} \frac{Ne^2}{m^*\epsilon_0}}. \quad (42)$$

Equation (41) takes the same functional form as the surface plasmon response of equation (23). Furthermore the resonant frequency ω_0 exhibits the same dependence on $\sqrt{N}$ as the surface plasmon response.

5.5. Monte Carlo modelling

Monte Carlo simulations allow the conductivity to be modelled by simulating the motion of individual charge carriers. Within the simulation it is possible to include specific microscopic parameters that influence charge carrier transport, such as nanowire boundaries and charge localisation within nanowires. It is also possible to simulate accurately the energetic distribution of charge carriers and the energy dependence of these carrier scattering rates, which significantly influence conductivity at high doping densities and highly non-equilibrium charge carrier distributions. Ponseca et al used Monte Carlo simulations to calculate the mobility spectra $\mu(\omega)$ of heavily n-doped InP nanowires for which the Fermi energy lies high in the conduction band [63]. The mobility spectra are related to conductivity spectra via $\sigma(\omega) = Ne\mu(\omega)$. Monte Carlo simulations enabled accurate modelling of carrier backscattering at the nanowire surfaces and good fits to the experimental data, with simulated mobility spectra (figure 15) featuring a negative imaginary part at THz frequencies.
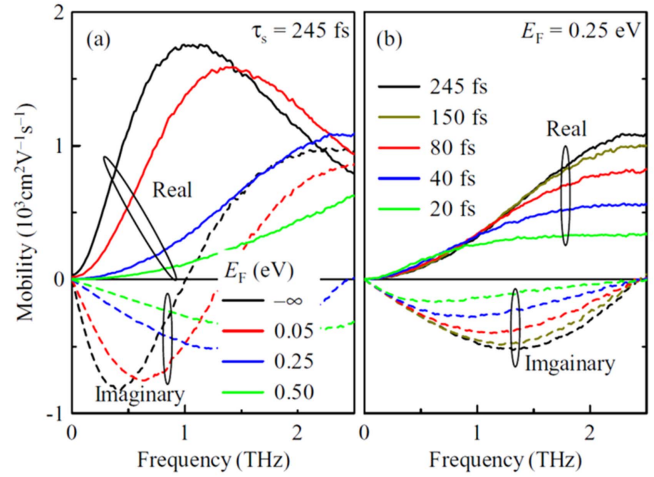
Figure 15. Electron mobility spectra calculated via Monte Carlo simulations of electron transport in InP nanowires with (a) different Fermi energies E_F and (b) different electron mean scattering times $\tau_s = \gamma^{-1}$. Reprinted with permission from [63]. Copyright 2014 by the American Physical Society.

5.6. Other models

It should be noted that numerous other models exist for the analysis of THz conductivity spectra. The models described above are those most commonly employed in studies of nanowires at room temperature. To date, most nanowires studied feature diameters too large to exhibit quantum confinement effects. However, quantum confinement effects can be anticipated if the nanowire diameter is reduced below the Bohr exciton radius or if quantum wells or dots are incorporated within the nanowires. In addition, excitonic effects can be anticipated at lower temperatures. Excellent reviews by Ulbricht et al [37] and Lloyd-Hughes [42] describe other models that can be applicable.

6. Electrical properties of nanowires probed by THz conductivity spectroscopy

THz-TDS and OPTP have revealed a wealth of information on a wide variety of semiconductor nanowires. In this section we highlight some key examples. Table 1 summarises electron lifetimes τ and surface recombination velocities S obtained via OPTP studies of various nanowires. Table 2 summarises electron mobilities μ, electron momentum scattering times γ^{-1}, and native electron concentrations due to doping N_{eq} obtained via THz-TDS and OPTP studies.

6.1. ZnO nanowires

One of the first THz studies of nanowires was performed by Baxter and Schmuttenmaer on ZnO nanowires [55]. The authors applied both THz-TDS and OPTP spectroscopy to compare the nanowires with nanoparticles and thin films, and to assess the effect of annealing. Measurements were performed with the nanowires standing vertically on their glass growth substrate. Conductivity and photoconductivity spectra

Table 1. Photoconductivity lifetimes (τ) and surface recombination velocities (S) measured via OPTP spectroscopy. A symbol '—' indicates that data has not been reported.

Nanowires	Diameter (nm)	Fabrication method	τ (ps)	S (cm s^{-1})	Reference
ZnO	100–200	Chemical bath deposition	$\tau_1 = 160$ $\tau_2 = 5600$	—	[55]
Ge	80	Au-catalysed, CVD	75–125	—	[44]
Si	30	Au-catalysed, CVD, annealed and etched	—	1.7×10^3	
Si	90	Au-catalysed, CVD, annealed	—	1.8×10^3	[57]
Si	90	Au-catalysed, CVD	—	1.1×10^3	
Si	110 ± 60	Au-catalysted, CVD	$\tau_1 = 2\text{–}4$ $\tau_2 = 4\text{–}10$	—	[53]
n-Si	90 ± 40		$\tau_1 = 0.6\text{–}1.4$ $\tau_2 = 16\text{–}37$	—	
GaAs	30		1.3		
	50	Au-catalysed, MOVPE	2.4	5.4×10^5	[49, 51]
	80		4.7		
InAs	27		200		
	45	Au-catalysed, MOVPE	290	3×10^3	[51]
	95		470		
	195		660		
InP	50		1180		
	85	Au-catalysed, MOVPE	1270	170	[50, 51]
	135		1300		
	160		1340		
GaAs/AlGaAs core–shell	50 nm core	Au-catalysed, MOVPE	5–1600	—	[46, 68]
n-GaAs	105		3800 ± 100	—	
p-GaAs	110	MBE	2500 ± 20	—	[69]
GaAs	115		130	—	
GaN	310	PAMBE	2500 ± 500	—	[71]

were calculated from raw data using the Bruggeman effective medium theory, and the spectra were fitted with the Drude–Smith model with parameter c_1 between -0.7 and -0.92. The measured signals were attributed to conduction electrons, rather than to holes, because the electron effective mass is much lower so that electrons contribute more strongly than holes to conductivity. Furthermore, ZnO is generally unintentionally n-type due to oxygen vacancies and zinc interstitials. The nanowires' photoconductivity decay featured an initial fast decay with a time constant of $\tau_1 = 160$ ps, followed by a slower decay with a time constant of $\tau_2 = 5.6$ ns. The as-grown nanowires featured a high native electron density $(1.9 \times 10^{18}$ cm$^{-3})$ at equilibrium. Annealing the nanowires was found to improve the electron mobility and reduce the native electron density, as annealing reduces the density of defects that give rise to n-type doping in ZnO. Interestingly, the electron mobility in the photoexcited nanowires (138 cm^2 V^{-1} s^{-1}) was significantly higher than the electron mobility in the nanowires at equilibrium (16 cm^2 V^{-1} s^{-1}). To explain this phenomenon the authors proposed that under photoexcitation a fraction of the excess

electrons fill deep traps, allowing the other electrons to move more freely.

6.2. Ge nanowires

Strait *et al* [44] investigated the ultrafast electrical properties of Ge nanowires using OPTP spectroscopy. The nanowires were grown by chemical vapour deposition (CVD) and transferred to quartz crystal substrates using a contact printing method that enables alignment of the wires horizontally on the substrate. Photoexcitation was performed at 780 nm, which generates electrons and holes near the Γ-point. Upon photoexcitation, the nanowire photoconductivity rose with a time constant of 1.7 ps. This time constant was interpreted as the average intraband relaxation time associated with hole cooling to the Γ-valley in the valence band, and electron scattering to the L-valley in the conduction band. The photoconductivity decayed with recombination time constants between 75 and 125 ps. The recombination rates were considerably faster compared to bulk Ge, attributed to the strong influence of surface recombination in the nanowires. Photoconductivity spectra were analysed using a surface plasmon model considering a net contribution

Table 2. Charge carrier scattering times γ^{-1}, mobilities μ and equilibrium electron concentrations N_{eq} in nanowires measured by THz-TDS and OPTP spectroscopy. The model used to extract the data is listed, with abbreviation 'DS' for Drude–Smith. A symbol '—' indicates that data has not been reported.

Nanowires	Diameter (nm)	Technique	γ^{-1} (fs)	μ (cm^{2}V^{-1} s^{-1})	N_{eq} (cm^{-3})	Model	Reference
ZnO	100–200	THz-TDS	28	16	19×10^{17}	DS	
ZnO	100–200	OPTP	84	138	—	DS	[55]
ZnO annealed	100–200	OPTP	88	189	—	DS	
SnO$_2$	50–100	OPTP	75 ± 7	72 ± 10	$(3.3 \pm 0.4) \times 10^{16}$	DS	[72]
SnO$_2$	100	THz-TDS	50	20	8×10^{16}	DS	[73]
In-Sn-O	50–100	THz-TDS	60–69	2–26	$(7–8) \times 10^{19}$	DS	[74]
Ge	80	OPTP	70 ± 15	1590	—	Plasmon	[44]
Si annealed	30	OPTP	—	60 ± 0.5	—	DS	
Si annealed	90	OPTP	—	38 ± 0.4	—	DS	[57]
Si	90	OPTP	—	13 ± 0.2	—	DS	
p-Si	90	THz-TDS	23.6–113.9	—	—	DS	[66]
Si	110 ± 60	OPTP	28 ± 6	190 ± 40	—	Plasmon	[53]
n-Si	90 ± 40	OPTP	14 ± 4	95 ± 25	$(5 \pm 3) \times 10^{17}$	Plasmon	
GaAs	50	OPTP	38 ± 4	1000 ± 100	$<10^{15}$	Plasmon	[49, 51]
InAs	45	OPTP	75 ± 12	6000 ± 1000	$(5 \pm 2) \times 10^{15}$	Plasmon	[51]
InAs	—	OPTP	22–71	—	—	Plasmon	[75]
InP	50	OPTP	32 ± 5	700 ± 100	$(10 \pm 3) \times 10^{15}$	Plasmon	
InP	85	OPTP	5.5	120	—	Plasmon	
InP	135	OPTP	10	220	—	Plasmon	[50, 51]
InP	160	OPTP	22	480	—	Plasmon	
n-InP	150	OPTP	>150	>3000	—	Monte Carlo	[63]
GaAs/AlGaAs core–shell	50 nm core	OPTP	46–115	1200–3000	—	Plasmon	[46, 68]
GaN	310	OPTP	—	820 ± 120	—	Plasmon	[71]
InN	130	THz-TDS	13 ± 0.2	80 ± 5	$(4.9 \pm 0.2) \times 10^{19}$	DS	[56]

from both electrons and holes. Fits yielded carrier momentum scattering times of 70 ± 15 fs and an effective carrier mobility of $1590 \, \mathrm{cm}^2 \, \mathrm{V}^{-1} \, \mathrm{s}^{-1}$. The authors noted a strong dependence of the THz response on the polarisation of the THz pulse relative to the nanowire orientation. Transmission of the THz pulse was attenuated most strongly when the THz electric field was oriented parallel to the nanowires, and almost negligibly when the THz electric field was polarised perpendicular to the nanowire axes.

6.3. Si nanowires

The properties of silicon nanowires have been measured in independent studies by Ulbricht *et al* [65], Lim *et al* [66], Bergren *et al* [57] and Beaudoin *et al* [53].

Ulbricht and co-authors investigated 25 nm diameter Si nanowires etched from a p-type Si substrate [65]. They used OPTP spectroscopy to investigate charge diffusion from the nanowires to the underlying Si substrate and charge trapping at nanowire surfaces. Their approach utilised the very different spectral shapes of the nanowire conductivity and the underlying substrate conductivity, which are Lorentzian and Drude-like respectively. Photoconductivity spectra taken between 10 and 400 ps after photoexcitation were therefore fitted with both a Lorentzian contribution and a Drude contribution. The Lorentzian contribution decayed after photoexcitation whereas the Drude component increased, signifying the transfer of charges from the nanowires to the substrate. Photoconductivity decays obtained at different excitation fluences were fitted with a time-dependent

diffusion model, yielding a nanowire surface trap density of $4.5 \pm 1.5 \times 10^9 \, \text{cm}^{-2}$. Annealing the nanowires under forming gas reduced the trap density to $(2 \pm 1) \times 10^9 \, \text{cm}^{-2}$ via surface passivation. The measurements revealed that at the lowest photoexcitation densities, the majority of the carriers are trapped at surface defects before they can diffuse to the substrate.

The conductivity of p-type Si nanowires was investigated using THz-TDS by Lim *et al* [66]. These 90 nm diameter nanowires were etched from a p-type Si substrate and measurements were performed with the nanowires standing vertically on this parent substrate. Transmission spectra were measured with the THz pulse incident at angles of 0° and 40° to the surface normal. This enabled determination of the transverse and longitudinal conductivities: the conductivities perpendicular and parallel to the nanowire axes respectively. The transverse conductivity spectrum was fitted with the Drude–Smith model yielding a scattering time γ_{DS}^{-1} of 113.9 fs. The longitudinal conductivity spectrum was fitted with a Lorentzian function and a scattering time of 23.6 fs was obtained. The difference in scattering times was attributed to the influence of surface scattering.

Bergren *et al* [57] measured Si nanowires grown by CVD using Au catalysts. Three samples were compared: as-grown nanowires (90 nm diameter), nanowires annealed under argon atmosphere (90 nm diameter), and nanowires annealed, thermally oxidised and HF- etched (30 nm diameter). The nanowires were mechanically removed from the substrate and dispersed in chloroform for OPTP measurements. Surface recombination velocities were determined from the measured photoconductivity decays. The surface recombination velocity was lowest for the as-grown nanowires $(1098 \pm 36 \, \text{cm} \, \text{s}^{-1})$ and higher for the annealed nanowires, at $1665 \pm 24 \, \text{cm} \, \text{s}^{-1}$ for the 30 nm annealed nanowires and $1768 \pm 30 \, \text{cm} \, \text{s}^{-1}$ for the 90 nm annealed nanowires. Photoconductivity spectra were extracted from raw data using an effective medium approximation and analysed with the Drude–Smith model with parameter c_1 between -0.85 and -0.95. The 30 nm diameter nanowires exhibited mobility values between 60 and 900 $\text{cm}^2 \, \text{V}^{-1} \, \text{s}^{-1}$, where the mobility decreased with increasing carrier density due to increased carrier–carrier scattering. Annealing increased the carrier mobility but also increased the surface recombination velocity, which was attributed to the presence of Au atoms on the nanowire surfaces after annealing.

The effect of n-doping on Si nanowires was investigated by Beaudoin *et al* [53]. The nanowires were grown on quartz substrates by CVD using Au catalysts. Undoped nanowires and nanowires n-doped with phosphorus were compared using OPTP spectroscopy. Photoconductivity decays exhibited biexponential behaviour with time constants of the order of picoseconds. Decays for the n-doped nanowires were nearly fluence-independent whereas decays for the undoped nanowires slowed at the highest fluences due to the saturation of trap states. Photoconductivity spectra were fitted with a Drude–plasmon model following equations (25)–(27). For the undoped sample, N_{eq} was set to zero and a scattering time of $28 \pm 6 \, \text{fs}$ and electron mobility of $190 \pm 40 \, \text{cm}^2 \, \text{V}^{-1} \, \text{s}^{-1}$

were determined from the fit. Fitting the spectra obtained from the n-doped sample yielded a scattering time of $14 \pm 4 \, \text{fs}$, a electron mobility of $95 \pm 25 \, \text{cm}^2 \, \text{V}^{-1} \, \text{s}^{-1}$ and a doping carrier density of $N_{\text{eq}} = (5 \pm 3) \times 10^{17} \, \text{cm}^{-3}$. Doping was found to reduce the photocarrier mobility and this effect was attributed to the role of ionised dopants as scattering centres.

6.4. GaAs nanowires and GaAs/AlGaAs core–shell nanowires

The THz conductivity of GaAs nanowires was first investigated by Parkinson *et al* using OPTP spectroscopy [49]. The nanowires were grown by metalorganic vapour phase epitaxy (MOVPE) using Au nanoparticle catalysts to drive anisotropic nanowire growth. The nanowires exhibited a pronounced surface plasmon mode and a very short photoconductivity lifetime ($<10 \, \text{ps}$) due to rapid charge trapping at the nanowire surface [49]. By comparing the photoconductivity dynamics of bare GaAs nanowires of various diameters, the surface recombination velocity was determined to be extremely high, at $5.4 \times 10^5 \, \text{cm} \, \text{s}^{-1}$ [51].

We investigated the improvements afforded by passivating GaAs nanowires with AlGaAs shells and by eliminating twin defects from the GaAs cores [67, 68]. Overcoating with an AlGaAs shell was found to improve carrier lifetime by a factor of 4, and the elimination of twin defects enhanced the carrier lifetime by 176% [68]. For all samples, photoconductivity lifetimes increased with increasing excitation fluence, suggesting the existence of trap states that saturate at higher photoexcited carrier densities. The decays were therefore fitted using a pair of coupled rate equations describing the decay of free carriers and the filling of trap states. The fitting allowed determination of the trap density, which was found to be 82% lower in AlGaAs-coated nanowires than in bare GaAs nanowires. Photoconductivity spectra were fitted with a surface plasmon model, enabling determination of the electron mobility. The twin-free core–shell nanowire sample exhibited an electron mobility of $2250 \, \text{cm}^2 \, \text{V}^{-1} \, \text{s}^{-1}$, almost twice that of its twinned counterpart ($1200 \, \text{cm}^2 \, \text{V}^{-1} \, \text{s}^{-1}$). Our later study revealed that by optimising the AlGaAs shell growth conditions and thickness, surface-related scattering can be reduced significantly so that the electron mobility can reach bulk-like values of up to $3000 \, \text{cm}^2 \, \text{V}^{-1} \, \text{s}^{-1}$ [46]. The improvement in mobility was concomitant with an increase in photoconductivity lifetime, which reached up to 1.6 ns for nanowires with the thickest (34 nm) AlGaAs shells.

OPTP studies have also been used to study the electronic properties of doped GaAs nanowires. Modulation doped GaAs/AlGaAs core–shell nanowires grown by molecular beam epitaxy (MBE) were investigated by Boland *et al* [52]. A Si-doped layer was incorporated in the AlGaAs shell during growth. By fitting photoconductivity spectra with the surface plasmon model (equations (25)–(27)), a native electron concentration of $1.1 \times 10^{16} \, \text{cm}^{-3}$ was extracted, indicating the effectiveness of the modulation doping in introducing electrons into the GaAs nanowire core. The electron mobility, which was found to be as high as $2200 \pm 300 \, \text{cm}^2 \, \text{V}^{-1} \, \text{s}^{-1}$,
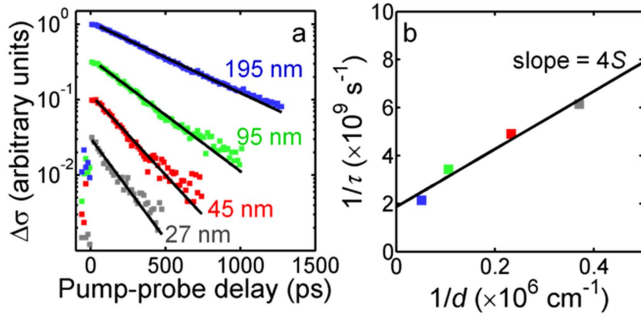
Figure 16. (a) Photoconductivity decays for 27, 45, 95 and 195 nm diameter InAs nanowires, fitted with carrier lifetimes of $\tau = 200$, 290, 470 and 660 ps respectively. Decays are scaled for clarity. (b) Plot of decay rate $1/\tau$ versus inverse nanowire diameter $1/d$. Data in (a) are reproduced with permission from [51]. Copyright 2013 Institute of Physics.

was not significantly degraded compared with undoped reference nanowires at similar carrier densities. The high mobility is retained because in modulation doped nanowires the charge carriers in the GaAs core are spatially separated from the ionised dopants, which would otherwise act as scattering centres. Both n- and p-type doping, achieved by growing doped GaAs shells around intrinsic GaAs nanowire cores, have been studied using OPTP spectroscopy [69]. In this study, photoconductivity spectra were fitted with a surface plasmon model that took into account the equilibrium electron and hole densities. The measured electron and hole densities exceeded $10^{18}\,\mathrm{cm}^{-3}$ for the n-doped and p-doped nanowires. The nanowires with the n-doped shells, p-doped shells and intrinsic shells featured electron mobilities of $460 \pm 63\,\mathrm{cm}^2\,\mathrm{V}^{-1}\,\mathrm{s}^{-1}$, $380 \pm 57\,\mathrm{cm}^2\,\mathrm{V}^{-1}\,\mathrm{s}^{-1}$ and $1700 \pm 270\,\mathrm{cm}^2\,\mathrm{V}^{-1}\,\mathrm{s}^{-1}$ respectively. The reduction in mobility for the doped samples was attributed to charge scattering with dopant impurities. The hole mobility in the p-doped nanowires was measured as $48 \pm 12\,\mathrm{cm}^2\,\mathrm{V}^{-1}\,\mathrm{s}^{-1}$. Furthermore, n-doped and p-doped nanowires exhibited long photoconductivity lifetimes of 3.8 and 2.5 ns, over an order of magnitude greater than that of the undoped nanowires (0.13 ns). These results indicate that doping can reduce the surface recombination velocity and may be used as an alternative to surface passivation for improving photoconductivity lifetimes.

6.5. InAs nanowires

Zinc-blende InAs nanowires grown by MOVPE and catalysed by Au nanoparticles have been investigated in our group using OPTP spectroscopy [51]. Photoconductivity decays were recorded for four samples of different average diameter (27, 45, 95 and 195 nm), as plotted in figure 16(a). The decays were monoexponential and the fitted lifetimes, τ, showed a strong systematic dependence on the nanowire diameter. Nanowires with narrower diameters exhibited shorter lifetimes due to the stronger influence of surface recombination. The surface recombination velocity S was extracted using this dependence of τ on nanowire diameter,

which follows the formula [70]:

$$\frac{1}{\tau} = \frac{1}{\tau_{\mathrm{volume}}} + \frac{4S}{d}, \tag{43}$$

where d is the nanowire diameter and τ_{volume} is the time constant for recombination within the nanowire volume. Fitting was performed as illustrated in figure 16(b) and from the slope of the plot, a surface recombination velocity of $3000\,\mathrm{cm}\,\mathrm{s}^{-1}$ was determined. Photoconductivity spectra measured for the 45 nm diameter nanowires showed a pronounced Lorentzian response typical of surface plasmon resonance. Spectra obtained at different photoexcited charge carrier densities were globally fitted using equations (25)–(27). This fitting enabled determination of the electron mobility of $6000\,\mathrm{cm}^2\,\mathrm{V}^{-1}\,\mathrm{s}^{-1}$ and the equilibrium electron concentration of $(5 \pm 2) \times 10^{15}\,\mathrm{cm}^{-3}$.

6.6. InP nanowires

OPTP measurements of InP nanowires have been performed by Ponseca *et al* [63] and by our group [50, 51].

Our group studied InP nanowires grown by MOVPE using Au catalysts and transferred to quartz substrates for THz measurements [50]. Long photoconductivity lifetimes of over 1 ns were measured for nanowires of average diameter of 50, 85, 135 and 160 nm. The lifetimes showed only a weak dependence on nanowire diameter indicating that the lifetime is relatively insensitive to surface states. By fitting the lifetime data with equation (43) a low surface recombination velocity of $170\,\mathrm{cm}\,\mathrm{s}^{-1}$ was determined [50]. Photoconductivity spectra were measured for nanowires of different diameters, from which electron mobilities between $120\,\mathrm{cm}^2\,\mathrm{V}^{-1}\,\mathrm{s}^{-1}$ and $660\,\mathrm{cm}^2\,\mathrm{V}^{-1}\,\mathrm{s}^{-1}$ were extracted using a surface plasmon fit. The electron mobility showed no systematic dependence on nanowire diameter, suggesting that scattering at nanowire surfaces is not the major factor limiting carrier mobility. Instead, stacking faults in these nanowires were identified as the major scattering mechanism limiting carrier mobility. In our later study we applied a global fit using equations (25)–(27) to spectra obtained from the 50 nm diameter nanowires at different photoexcited carrier densities [51]. This fitting enabled us to extract the equilibrium electron concentration due to unintentionally incorporated donors $((10 \pm 3) \times 10^{15}\,\mathrm{cm}^{-3})$.

In their work, Ponseca and co-authors measured a periodic array of 150 nm diameter heavily n-doped InP nanowires embedded in an electrically insulating polydimethylsiloxane (PDMS) polymer matrix [63]. These nanowires were grown via MOVPE using Au catalysts. The nanowire axes were oriented parallel to THz propagation direction and perpendicular to the THz electric field, so that the OPTP measurements probed the conductivity perpendicular to the nanowire axis, that is, the transverse conductivity. Photoconductivity spectra obtained 10 ps after photoexcitation were fitted with a Monte Carlo model that accounted for electron localisation and heavy doping. The fit revealed a long scattering time of over 150 fs, corresponding to a transverse electron mobility of over $3000\,\mathrm{cm}^2\,\mathrm{V}^{-1}\,\mathrm{s}^{-1}$. This value is significantly larger than

reported longitudinal mobilities, including those measured using previous OPTP measurements, as transverse transport is unaffected by the stacking faults along the growth direction that limit longitudinal transport.

6.7. GaN nanowires

Parkinson *et al* [71] investigated GaN nanowires using OPTP spectroscopy. The GaN nanowires were grown by plasma-assisted MBE (PAMBE) and then transferred to quartz substrates for THz measurements. The measured nanowire photoconductivity lifetime (2.5 ± 0.5 ns) significantly exceeded the lifetime measured for high quality bulk GaN. Spectra were fitted with a surface plasmon model, with which the electron mobility of $820 \pm 120 \, \mathrm{cm^2 \, V^{-1} \, s^{-1}}$ was extracted. This electron mobility also exceeded the value determined for bulk GaN ($590 \pm 50 \, \mathrm{cm^2 \, V^{-1} \, s^{-1}}$). The superior electrical properties of the nanowires compared to bulk were attributed to the strain-free and dislocation-free nature of the nanowires.

6.8. InN nanorods

Ahn *et al* performed THz-TDS measurements of InN nanorods grown by PAMBE [56]. The measurements were obtained with the nanorods standing vertically on their Si growth substrate. Conductivity spectra of nanorods were calculated considering the average permittivity over the sample volume: $\epsilon_l = f\epsilon_{nw} + (1-f)\epsilon_h$. The spectra were fitted with the Drude–Smith model with parameter c_1 of -0.65 ± 0.01, yielding a native electron density of $(4.9 \pm 0.2) \times 10^{19} \, \mathrm{cm^{-3}}$, a scattering time of 13 ± 0.2 fs and a mobility of $80 \pm 5 \, \mathrm{cm^2 \, V^{-1} \, s^{-1}}$. The mobility in the nanorods was over an order of magnitude lower than the mobility in InN films. The low mobility of the nanorods samples was tentatively attributed to the restriction of lateral electron transport within and between the isolated nanorods.

7. Studying single nanowires

The spatial resolution achievable using THz spectroscopy is limited by the spot size of the THz probe, and is theoretically limited by diffraction to a feature size of $\lambda/2$. The theoretical limit corresponds to $150 \, \mu m$ at a frequency of 1 THz, and practical spot sizes in conventional THz systems are of the order of 1 mm. This large spot size restricts conventional THz spectroscopy measurements, such as those described in section 6, to ensembles of nanowires and precludes measurements of single nanowires. Near-field techniques have gained significant attention for their ability to improve the spatial resolution of THz spectroscopic measurements beyond the diffraction limit [76]. These techniques can involve, for example, a subwavelength-sized aperture to reduce the size of the THz source or detector, or a subwavelength-sized metallic tip to scatter near-field radiation. An excellent review by Adam [77] describes these near-field techniques in detail.

Recently, Eisele and co-workers [75] developed an innovative near-field technique for performing multi-THz
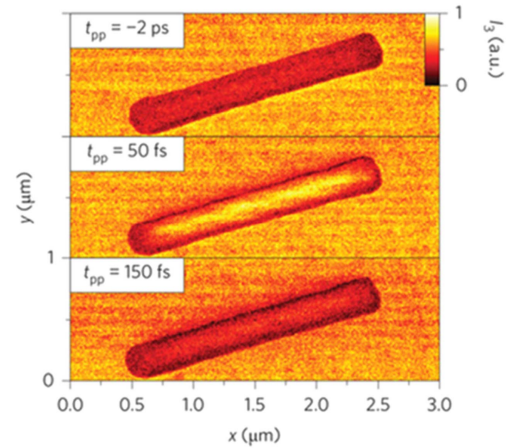
Figure 17. Intensity maps of THz radiation scattered from an InAs nanowire at times 2 ps before photoexcitation and 50 and 150 fs after photoexcitation. These images were obtained by coupling THz pulses to the apex of a metallic tip. Reprinted by permission from Macmillan Publishers Ltd: [75], copyright 2014.

spectroscopy on single Se-doped n-type InAs nanowires. The technique combined OPTP spectroscopy with scattering-type near-field scanning optical microscopy (s-NSOM) operated in tapping mode. Pulses (of bandwidth 20–45 THz) were coupled to the apex of the metallic tip of the s-NSOM, which confines the radiation to the near field. The scattered pulses encode information on the local dielectric and conductivity properties of the sample with a spatial resolution of 10 nm. This technique was used to probe charge carrier dynamics in a single photoexcited InAs nanowire (figure 17). The tapping amplitude was used to control the probing depth into the sample, which enabled studies of the nanowire dielectric function in all three spatial dimensions. The results revealed that the carrier density is homogeneous immediately following photoexcitation, after which a depletion layer forms at the nanowire surface within 50 fs. The carrier population was observed to decay on a picosecond timescale due to trapping at defect states.

8. Outlook and conclusion

THz spectroscopy is a powerful non-contact probe, capable of measuring carrier transport and dynamics with sub-picosecond temporal resolution. It is therefore ideally suited to studies of semiconductor nanowires. We have discussed how ac and dc transport parameters, such as charge carrier mobility, lifetime, surface recombination and ionised dopant densities, can be elucidated using THz-TDS and OPTP measurements.

We conclude this review with a discussion of how THz measurements are guiding the development of nanowire-based devices. Our specific example is that of photoconductive THz receivers based on single nanowires, as designed by Peng *et al* and illustrated in figure 18 [78]. Three samples of GaAs/AlGaAs/GaAs core–shell–cap nanowires were investigated. One of these samples featured a twin-free
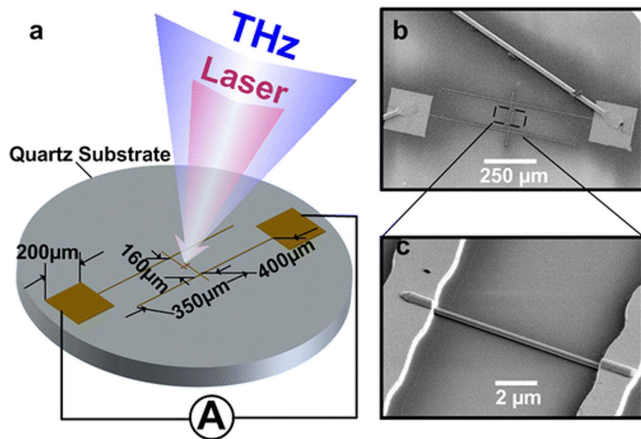
Figure 18. (a) Schematic of the photoconductive detector with incident THz and optical photoexcitation pulses. (b) SEM image of a fabricated device. (c) Magnified SEM image of the central area of the device showing the nanowire. Reprinted with permission from [78]. Copyright 2015 American Chemical Society.

zinc-blende core and a 28 nm thick AlGaAs shell. OPTP measurements revealed that this sample featured the highest charge carrier mobility and lifetime (4.6 ns), owing to the elimination of twin defects in the GaAs core [68] and optimisation of the AlGaAs shell thickness [46]. It was anticipated, therefore, that this sample would show the strongest sensitivity of THz detection. In excellent agreement, the device based on this sample showed the largest photo-current and greatest THz-induced current flow. The above is just one example of device design directed by THz mea-surements, which demonstrates how THz measurements provide unprecedented insight into device-relevant electrical properties with extremely high throughput and accuracy.

THz spectroscopy is today so well-developed that it may be used to probe complex nanowire structures, such as axial and radial nanowire heterostructures, doped nanowires with p–n junctions, and zinc-blende/wurtzite polytypic nanowires. The field of THz spectroscopy continues to progress rapidly and we can look forward to exciting developments and improvements in the near future. For example, advances in THz near-field techniques will potentially enable the study of the electrical properties of increasingly complex nanowires with sub-micron spatial resolution, without invoking effective medium theories. These advances may be achieved by extending the promising s-NSOM tools developed by Eisele et al [75] to the conventional THz range (0.1–10 THz). Recently developed techniques for improving the bandwidth of the THz spectrometers [79] are anticipated to enable investigation of both longitudinal and transverse transport, that is, transport parallel and perpendicular to the nanowire axis, in a single experiment. To date the majority of THz studies have focussed on the longitudinal response occurring between 0.1 and 4 THz, whereas signatures of transverse transport lie at higher frequencies. Both transport directions are important in nanowire devices, with transverse transport particularly important for core–shell nanowire devices. A further prospect is the use of THz cyclotron resonance

measurements, which should reveal the carrier effective masses in nanowires with novel crystal phases, such as wurtzite InAs and wurtzite GaAs nanowires [80].

It is clear that THz spectroscopy has a promising future in guiding the development of nanowires for an enormous variety of device applications.

Acknowledgments

References

[1] Dayeh S A et al 2013 Direct measurement of coherency limits for strain relaxation in heteroepitaxial core/shell nanowires Nano Lett. **13** 1869–76

[2] Kelzenberg M D, Boettcher S W, Petykiewicz J A, Turner-Evans D B, Putnam M C, Warren E L, Spurgeon J M, Briggs R M, Lewis N S and Atwater H A 2010 Enhanced absorption and carrier collection in Si wire arrays for photovoltaic applications Nat. Mater. **9** 239

[3] Reimer M E, Bulgarini G, Akopian N, Hocevar M, Bavinck M B, Verheijen M A, Bakkers E P, Kouwenhoven L P and Zwiller V 2012 Bright single-photon sources in bottom-up tailored nanowires Nat. Commun. **3** 737

[4] Bulgarini G, Reimer M E, Bouwes Bavinck M, Jons K D, Dalacu D, Poole P J, Bakkers E P and Zwiller V 2014 Nanowire waveguides launching single photons in a Gaussian mode for ideal fiber coupling Nano Lett. **14** 4102–6

[5] Wallentin J et al 2013 InP nanowire array solar cells achieving 13.8% efficiency by exceeding the ray optics limit Science **339** 1057–60

[6] Krogstrup P, Jørgensen H I, Heiss M, Demichel O, Holm J V, Aagesen M, Nygard J and Fontcuberta i Morral A 2013 Single-nanowire solar cells beyond the Shockley–Queisser limit Nat. Photon. **7** 306–10

[7] Yao M, Cong S, Arab S, Huang N, Povinelli M L, Cronin S B, Dapkus P D and Zhou C 2015 Tandem solar cells using GaAs nanowires on Si: design, fabrication, and observation of voltage addition Nano Lett. **15** 7217–24

[8] Heiss M et al 2013 Self-assembled quantum dots in a nanowire system for quantum photonics Nat. Mater. **12** 439–44

[9] Holmes M J, Choi K, Kako S, Arita M and Arakawa Y 2014 Room-temperature triggered single photon emission from a III-nitride site-controlled nanowire quantum dot Nano Lett. **14** 982–6

[10] Vitiello M S, Coquillat D, Viti L, Ercolani D, Teppe F, Pitanti A, Beltram F, Sorba L, Knap W and Tredicucci A 2012 Room-temperature terahertz detectors based on semiconductor nanowire field-effect transistors Nano Lett. **12** 96–101

[11] Saxena D, Mokkapati S, Parkinson P, Jiang N, Gao Q, Tan H H and Jagadish C 2013 Optically pumped room-temperature GaAs nanowire lasers Nat. Photon. **7** 963–8

[12] Sidiropoulos T P H, Röder R, Geburt S, Hess O, Maier S A, Ronning C and Oulton R F 2014 Ultrafast plasmonic nanowire lasers near the surface plasmon frequency Nat. Phys. **10** 870–6

[13] Tomioka K, Yoshimura M and Fukui T 2012 A III–V nanowire channel on silicon for high-performance vertical transistors *Nature* **488** 189–92

[14] Das A, Ronen Y, Most Y, Oreg Y, Heiblum M and Shtrikman H 2012 Zero-bias peaks and splitting in an Al–InAs nanowire topological superconductor as a signature of Majorana fermions *Nat. Phys.* **8** 887–95

[15] Mourik V, Zuo K, Frolov S M, Plissard S R, Bakkers E P A M and Kouwenhoven L P 2012 Signatures of majorana fermions in hybrid superconductor-semiconductor nanowire devices *Science* **336** 1003–7

[16] Storm K, Halvardsson F, Heurlin M, Lindgren D, Gustafsson A, Wu P M, Monemar B and Samuelson L 2012 Spatially resolved Hall effect measurement in a single semiconductor nanowire *Nat. Nano* **7** 718–22

[17] van Tilburg J W W, Algra R E, Immink W G G, Verheijen M, Bakkers E P A M and Kouwenhoven L P 2010 Surface passivated InAs/InP core/shell nanowires *Semicond. Sci. Technol.* **25** 024011

[18] Bertness K A, Sanford N A and Davydov A V 2011 GaN nanowires grown by molecular beam epitaxy *Sel. Top. Quantum Electron.* **17** 847–58

[19] Dayeh S A, Soci C, Yu P K L, Yu E T and Wang D 2007 Transport properties of InAs nanowire field effect transistors: the effects of surface states *J. Vac. Sci. Technol.* B **25** 1432

[20] Wunnicke O 2006 Gate capacitance of back-gated nanowire field-effect transistors *Appl. Phys. Lett.* **89** 083102

[21] Wallentin J, Ek M, Wallenberg L R, Samuelson L and Borgstrom M T 2012 Electron trapping in InP nanowire FETs with stacking faults *Nano Lett.* **12** 151–5

[22] Hultin O, Otnes G, Borgstrom M T, Bjork M, Samuelson L and Storm K 2016 Comparing Hall effect and field effect measurements on the same single nanowire *Nano Lett.* **16** 205–11

[23] Tu R, Zhang L, Nishi Y and Dai H 2007 Measuring the capacitance of individual semiconductor nanowires for carrier mobility assessment *Nano Lett.* **7** 1561–5

[24] Roddaro S, Nilsson K, Astromskas G, Samuelson L, Wernersson L-E, Karlström O and Wacker A 2008 InAs nanowire metal-oxide-semiconductor capacitors *Appl. Phys. Lett.* **92** 253509

[25] Zhao Y, Candebat D, Delker C, Zi Y, Janes D, Appenzeller J and Yang C 2012 Understanding the impact of Schottky barriers on the performance of narrow bandgap nanowire field effect transistors *Nano Lett.* **12** 5331–6

[26] Blömers C, Grap T, Lepsa M I, Moers J, Trellenkamp S, Grötzmacher D, Lüth H and Schäpers T 2012 Hall effect measurements on InAs nanowires *Appl. Phys. Lett.* **101** 152106

[27] Heurlin M, Hultin O, Storm K, Lindgren D, Borgstrom M T and Samuelson L 2014 Synthesis of doped InP core–shell nanowires evaluated using hall effect measurements *Nano Lett.* **14** 749–53

[28] Schmidt V, Mensch P F J, Karg S F, Gotsmann B, Das Kanungo P, Schmid H and Riel H 2014 Using the Seebeck coefficient to determine charge carrier concentration, mobility, and relaxation time in InAs nanowires *Appl. Phys. Lett.* **104** 012113

[29] Tchoulfian P, Donatini F, Levy F, Amstatt B, Dussaigne A, Ferret P, Bustarret E and Pernot J 2013 Thermoelectric and micro-Raman measurements of carrier density and mobility in heavily Si-doped GaN wires *Appl. Phys. Lett.* **103** 202101

[30] Roddaro S, Ercolani D, Safeen M A, Suomalainen S, Rossella F, Giazotto F, Sorba L and Beltram F 2013 Giant thermovoltage in single InAs nanowire field-effect transistors *Nano Lett.* **13** 3638–42

[31] Thelander C, Björk M T, Larsson M W, Hansen A E, Wallenberg L R and Samuelson L 2004 Electron transport in InAs nanowires and heterostructure nanowire devices *Solid State Commun.* **131** 573–9

[32] Bjork M T, Schmid H, Knoch J, Riel H and Riess W 2009 Donor deactivation in silicon nanostructures *Nat. Nano* **4** 103–7

[33] Durand C, Berthe M, Makoudi Y, Nys J P, Leturcq R, Caroff P and Grandidier B 2013 Persistent enhancement of the carrier density in electron irradiated InAs nanowires *Nanotechnology* **24** 275706

[34] Ketterer B, Uccelli E and Fontcuberta i Morral A 2012 Mobility and carrier density in p-type GaAs nanowires measured by transmission Raman spectroscopy *Nanoscale* **4** 1789–93

[35] Seo M A, Yoo J, Dayeh S A, Picraux S T, Taylor A J and Prasankumar R P 2012 Mapping carrier diffusion in single silicon core–shell nanowires with ultrafast optical microscopy *Nano Lett.* **12** 6334–8

[36] Lockwood D J, Yu G and Rowell N L 2005 Optical phonon frequencies and damping in AlAs, GaP, GaAs, InP, InAs and InSb studied by oblique incidence infrared spectroscopy *Solid State Commun.* **136** 404–9

[37] Ulbricht R, Hendry E, Shan J, Heinz T F and Bonn M 2011 Carrier dynamics in semiconductors studied with time-resolved terahertz spectroscopy *Rev. Mod. Phys.* **83** 543–86

[38] Schmuttenmaer C A 2004 Exploring dynamics in the far-infrared with terahertz spectroscopy *Chem. Rev.* **104** 1759–79

[39] Löffler T, Kreß M, Thomson M, Hahn T, Hasegawa N and Roskos H G 2005 Comparative performance of terahertz emitters in amplifier-laser-based systems *Semicond. Sci. Technol.* **20** S134–41

[40] Shan J, Nahata A and Heinz T F 2002 Terahertz time-domain spectroscopy based on nonlinear optics *J. Nonlinear Opt. Phys. Mater.* **11** 31–48

[41] Withayachumnankul W, Ferguson B, Rainsford T, Mickan S P and Abbott D 2005 Simple material parameter estimation via terahertz time-domain spectroscopy *Electron. Lett.* **41** 800

[42] Lloyd-Hughes J and Jeon T-I 2012 A Review of the terahertz conductivity of bulk and nano-materials *J. Infrared Millim. Terahz. Waves* **33** 871–925

[43] Beard M C, Turner G M and Schmuttenmaer C A 2000 Transient photoconductivity in GaAs as measured by time-resolved terahertz spectroscopy *Phys. Rev.* B **62** 15764–77

[44] Strait J H, George P A, Levendorf M, Blood-Forsythe M, Rana R and Park J 2009 Measurements of the carrier dynamics and terahertz response of oriented germanium nanowires *Nano Lett.* **9** 2967–72

[45] Kužel P, Kadlec F and Němec H 2007 Propagation of terahertz pulses in photoexcited media: analytical theory for layered systems *J. Chem. Phys.* **127** 024506

[46] Joyce H J, Parkinson P, Jiang N, Docherty C J, Gao Q, Tan H H, Jagadish C, Herz L M and Johnston M B 2014 Electron mobilities approaching bulk limits in 'surface-free' GaAs nanowires *Nano Lett.* **14** 5989–94

[47] Kužel P and Němec H 2014 Terahertz conductivity in nanoscaled systems: effective medium theory aspects *J. Phys. D: Appl. Phys.* **47** 374005

[48] Nienhuys H-K and Sundström V 2005 Influence of plasmons on terahertz conductivity measurements *Appl. Phys. Lett.* **87** 012101

[49] Parkinson P, Lloyd-Hughes J, Gao Q, Tan H H, Jagadish C, Johnston M B and Herz L M 2007 Transient terahertz conductivity of GaAs nanowires *Nano Lett.* **7** 2162–5

[50] Joyce H J *et al* 2012 Ultralow surface recombination velocity in InP nanowires probed by terahertz spectroscopy *Nano Lett.* **12** 5325–30

[51] Joyce H J, Docherty C J, Gao Q, Tan H H, Jagadish C, Lloyd-Hughes J, Herz L M and Johnston M B 2013 Electronic properties of GaAs, InAs and InP nanowires studied by terahertz spectroscopy *Nanotechnology* **24** 214006

[52] Boland J L *et al* 2015 Modulation doping of GaAs/AlGaAs core–shell nanowires with effective defect passivation and high electron mobility *Nano Lett.* **15** 1336−42

[53] Beaudoin A, Salem B, Baron T, Gentile P and Morris D 2014 Impact of n-type doping on the carrier dynamics of silicon nanowires studied using optical-pump terahertz-probe spectroscopy *Phys. Rev.* B **89** 115316

[54] Smith N 2001 Classical generalization of the Drude formula for the optical conductivity *Phys. Rev.* B **64** 155106

[55] Baxter J B and Schmuttenmaer C A 2006 Conductivity of ZnO nanowires, nanoparticles, and thin films using time-resolved terahertz spectroscopy *J. Phys. Chem.* B **110** 25229–39

[56] Ahn H, Ku Y P, Wang Y C, Chuang C H, Gwo S and Pan C-L 2007 Terahertz spectroscopic study of vertically aligned InN nanorods *Appl. Phys. Lett.* **91** 163105

[57] Bergren M R, Kendrick C E, Neale N R, Redwing J M, Collins R T, Furtak T E and Beard M C 2014 Ultrafast electrical measurements of isolated silicon nanowires and nanocrystals *J. Phys. Chem. Lett.* **5** 2050−7

[58] Němec H, Kužel P and Sundström V 2009 Far-infrared response of free charge carriers localized in semiconductor nanoparticles *Phys. Rev.* B **79** 115309

[59] Garnett J C M 1906 Colours in metal glasses, in metallic films, and in metallic solutions: II. *Phil. Trans. R. Soc.* A **205** 237–88

[60] Bruggeman D A G 1936 Berechnung verschiedener physikalischer Konstanten von heterogenen Substanzen: II. Dielektrizitätskonstanten und Leitfähigkeiten von Vielkristallen der nichtregulären systeme *Ann. Phys.* **417** 645–72

[61] Tinga W R 1973 Generalized approach to multiphase dielectric mixture theory *J. Appl. Phys.* **44** 3897

[62] Landauer R 1978 Electrical conductivity in inhomogeneous media *AIP Conf. Proc.* **40** 2–45

[63] Ponseca C S, Němec H, Wallentin J, Anttu N, Beech J P, Iqbal A, Borgström M, Pistol M E, Samuelson L and Yartsev A 2014 Bulk-like transverse electron mobility in an array of heavily n-doped InP nanowires probed by terahertz spectroscopy *Phys. Rev.* B **90** 085405

[64] Hendry E, Koeberg M, O'Regan B and Bonn M 2006 Local field effects on electron transport in nanostructured TiO_2 revealed by terahertz spectroscopy *Nano Lett.* **6** 755−9

[65] Ulbricht R, Kurstjens R and Bonn M 2012 Assessing charge carrier trapping in silicon nanowires using picosecond conductivity measurements *Nano Lett.* **12** 3821−7

[66] Lim M, Choi S-J, Lee G-S, Seol M-L, Do Y, Choi Y-K and Han H 2012 Terahertz time-domain spectroscopy of anisotropic complex conductivity tensors in silicon nanowire films *Appl. Phys. Lett.* **100** 211102

[67] Joyce H J, Gao Q, Tan H H, Jagadish C, Kim Y, Zhang X, Guo Y and Zou J 2007 Twin-free uniform epitaxial GaAs nanowires grown by a two-temperature process *Nano Lett.* **7** 921–6

[68] Parkinson P, Joyce H J, Gao Q, Tan H H, Zhang X, Zou J, Jagadish C, Herz L M and Johnston M B 2009 Carrier lifetime and mobility enhancement in nearly defect-free core–shell nanowires measured using time-resolved terahertz spectroscopy *Nano Lett.* **9** 3349–53

[69] Boland J L, Casadei A, Tutuncuoglu G, Matteini F, Davies C L, Jabeen F, Joyce H J, Herz L M, Fontcuberta I M A and Johnston M B 2016 Increased photoconductivity lifetime in GaAs nanowires by controlled n-type and p-type doping *ACS Nano* **10** 4219–27

[70] Léonard F, Talin A A, Swartzentruber B S and Picraux S T 2009 Diameter-dependent electronic transport properties of Au-catalyst/Ge-nanowire Schottky diodes *Phys. Rev. Lett.* **102** 106805

[71] Parkinson P, Dodson C, Joyce H J, Bertness K A, Sanford N A, Herz L M and Johnston M B 2012 Noncontact measurement of charge carrier lifetime and mobility in GaN nanowires *Nano Lett.* **12** 4600−4

[72] Tsokkou D, Othonos A and Zervos M 2012 Carrier dynamics and conductivity of SnO_2 nanowires investigated by time-resolved terahertz spectroscopy *Appl. Phys. Lett.* **100** 133101

[73] Zou X, Luo J, Lee D, Cheng C, Springer D, Nair S K, Cheong S A, Fan H J and Chia E E M 2012 Temperature-dependent terahertz conductivity of tin oxide nanowire films *J. Phys. D: Appl. Phys.* **45** 465101

[74] Yang C-S, Chang C-H, Lin M-H, Yu P, Wada O and Pan C-L 2012 THz conductivities of indium-tin-oxide nanowhiskers as a graded-refractive-index structure *Opt. Express* **20** A441–51

[75] Eisele M, Cocker T L, Huber M A, Plankl M, Viti L, Ercolani D, Sorba L, Vitiello M S and Huber R 2014 Ultrafast multi-terahertz nano-spectroscopy with sub-cycle temporal resolution *Nat. Photon.* **8** 841−5

[76] Cocker T L, Jelic V, Gupta M, Molesky S J, Burgess J A J, Reyes G D L, Titova L V, Tsui Y Y, Freeman M R and Hegmann F A 2013 An ultrafast terahertz scanning tunnelling microscope *Nat. Photon.* **7** 620−5

[77] Adam A J L 2011 Review of near-field terahertz measurement methods and their applications *J. Infrared Millim. Terahz. Waves* **32** 976–1019

[78] Peng K *et al* 2015 Single nanowire photoconductive terahertz detectors *Nano Lett.* **15** 206−10

[79] Ho I C and Zhang X-C 2014 Application of broadband terahertz spectroscopy in semiconductor nonlinear dynamics *Front. Optoelectron.* **7** 220–42

[80] Joyce H J, Wong-Leung J, Gao Q, Tan H H and Jagadish C 2010 Phase perfection in zinc blende and wurtzite III-V nanowires using basic growth parameters *Nano Lett.* **10** 908–15